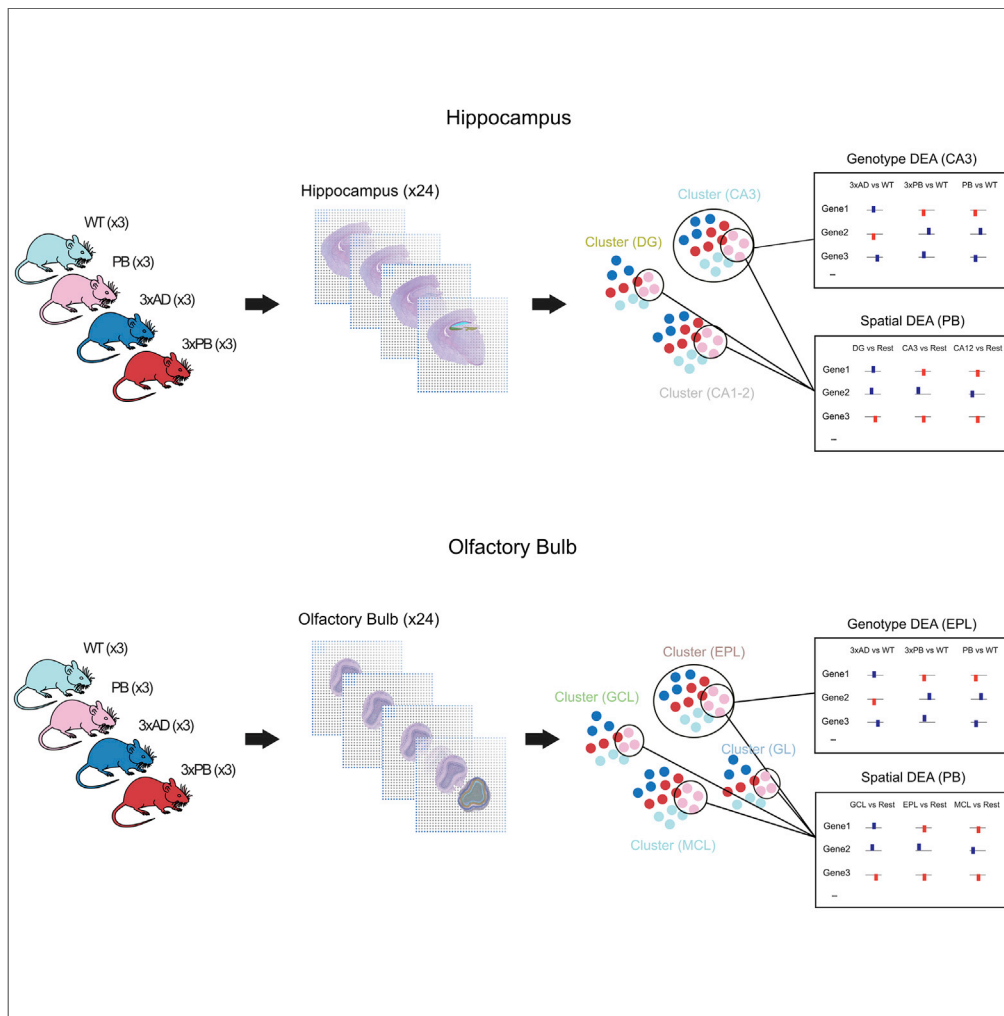


Article

Spatial Transcriptomics Reveals Genes Associated with Dysregulated Mitochondrial Functions and Stress Signaling in Alzheimer Disease



José Fernández Navarro, Deborah L. Croteau, Aleksandra Jurek, ..., Marie-Christine Galas, Joakim Lundeberg, Vilhelm A. Bohr

vbohr@nih.gov

HIGHLIGHTS

Spatial transcriptomics identifies differentially expressed genes with spatial patterns

Early application of spatial transcriptomics to olfactory bulbs from AD models

Bok gene is spatially differentially expressed in AD mouse and patient brains

Paip1 and *Homer1* genes are regulated in a PoB-dependent manner

Navarro et al., iScience 23, 101556
October 23, 2020
<https://doi.org/10.1016/j.isci.2020.101556>



Article

Spatial Transcriptomics Reveals Genes Associated with Dysregulated Mitochondrial Functions and Stress Signaling in Alzheimer Disease

José Fernández Navarro,^{1,6} Deborah L. Croteau,^{2,6} Aleksandra Jurek,¹ Zaneta Andrusivova,¹ Beimeng Yang,² Yue Wang,² Benjamin Ogedegbe,² Tahira Riaz,³ Mari Støen,³ Claus Desler,⁴ Lene Juel Rasmussen,⁴ Tone Tønjum,³ Marie-Christine Galas,⁵ Joakim Lundberg,^{1,7} and Vilhelm A. Bohr^{2,3,7,8,*}

SUMMARY

Alzheimer disease (AD) is a devastating neurological disease associated with progressive loss of mental skills and cognitive and physical functions whose etiology is not completely understood. Here, our goal was to simultaneously uncover novel and known molecular targets in the structured layers of the hippocampus and olfactory bulbs that may contribute to early hippocampal synaptic deficits and olfactory dysfunction in AD mice. Spatially resolved transcriptomics was used to identify high-confidence genes that were differentially regulated in AD mice relative to controls. A diverse set of genes that modulate stress responses and transcription were predominant in both hippocampi and olfactory bulbs. Notably, we identify *Bok*, implicated in mitochondrial physiology and cell death, as a spatially downregulated gene in the hippocampus of mouse and human AD brains. In summary, we provide a rich resource of spatially differentially expressed genes, which may contribute to understanding AD pathology.

INTRODUCTION

Alzheimer disease (AD) is a multifactorial and progressive neurodegenerative disorder that is the most common cause of dementia globally. Poor short-term memory and olfactory dysfunction are early signs in early stages of AD (Murphy, 2019; Rahayel et al., 2012). Emerging evidence suggests that olfactory dysfunction might predate the onset of cognitive decline. Often, olfactory dysfunction is perceived by the individual as a loss of taste, which worsens with the progression of the disease; however, the relationships between olfactory deficits, neurodegeneration, and dementia remain unclear (Murphy, 2019). Given the abundance of failed clinical trials for AD, it is apparent that neither the genes nor the cellular mechanisms that underlie this multifactorial disease are well understood. Hence, the molecular pathology of this devastating disorder is still in its infancy.

Genetically engineered mouse models are widely used to characterize molecular features of AD, including AD-associated differential gene expression. The triple transgenic AD model, 3xTg AD (3xAD), expresses three human gene variants: APP K670N/M671L, MAPT P301L, and PS1 M146V. Increased DNA damage occurs early in the course of AD disease pathology, and to test the importance of DNA repair, we created a modified version of the 3xAD strain by adding a deficiency in DNA polymerase beta (Polβ) (Sykora et al., 2015). Importantly, we had previously observed a loss of this protein and its polymerase activity in the brains of human patients with AD patient (Weissman et al., 2007). Behavioral and biochemical analyses of 3xTg AD/Polβ^{+/-} (3xPB) mice revealed that these mice display more severe deficits in memory, learning, long-term potentiation (LTP), olfactory function, and mitochondrial homeostasis and higher levels of DNA damage and cell death than control mice (Hou et al., 2018; Misiak et al., 2017a; Sykora et al., 2015).

Gene expression changes contribute to AD disease, and defining a more detailed map of how gene expression changes in the neuronal structures of the brain, early in the disease process, may contribute to a better understanding of the disorder. Thus, the goal of the present study was to identify spatially expressed genes that were differentially expressed (DE) in the hippocampal and olfactory bulb (OFB) regions of 3xAD, 3xPB, and control mice. To accomplish this goal, gene expression was quantified using a powerful

¹Science for Life Laboratory, Department of Gene Technology, KTH Royal Institute of Technology, 17165 Stockholm, Sweden

²Laboratory of Molecular Gerontology, National Institute on Aging, Baltimore, MD 21224, USA

³Unit for Genome Dynamics, Department of Microbiology, University of Oslo and Oslo University Hospital, 0372 Oslo, Norway

⁴Center for Healthy Aging, Department of Cellular and Molecular Medicine, University of Copenhagen, 2200 Copenhagen, Denmark

⁵University of Lille, Inserm, CHU Lille, UMR-S 1172 - Centre de Recherche Jean-Pierre AUBERT Neurosciences et Cancer, 59000 Lille, France

⁶These authors contributed equally

⁷These authors contributed equally

⁸Lead Contact

*Correspondence: vbohr@nih.gov

<https://doi.org/10.1016/j.isci.2020.101556>



method known as spatial transcriptomics (ST), recently described by Stahl and colleagues (Stahl et al., 2016). In earlier studies, ST was used to analyze differential gene expression in neuronal tissue in neurodegenerative diseases (Chen et al., 2020; Maniatis et al., 2019). The key feature of ST is that it pairs quantitative transcriptomics with high-resolution tissue imaging; this allows gene expression profiles to be anchored to the physical map of the organ or tissue(s) of interest, which in this study are the hippocampal and OFB regions of the brain. The hippocampus and OFB play central roles in AD pathology, and these anatomical brain regions are each composed of layers of specialized cells. Thus, we focused our gene expression analyses on these brain regions.

ST is an attractive approach to resolve spatial differences in gene expression in AD brains. ST is unique, yielding a substantially different, richer dataset than more traditional transcriptome analysis using gene expression microarray technology. It combines high-resolution tissue imaging with unbiased spatially defined RNA sequencing (RNA-seq) using barcoded spots (100 μm) on glass slides (Stahl et al., 2016). This affords the opportunity to characterize tissue morphology using unsupervised analyses at the molecular level. In comparison, previous RNA-seq of bulk brain tissue extracts is data rich but limited by the fact that it lacks spatial information. The alternative to bulk analysis is to perform single-cell/single-nuclei RNA-seq. However, this technique also does not yield spatial gene expression measures unless combined with fine dissection techniques. Furthermore, although the resolution of ST at the level of the spot is nominally lower than the resolution of single-cell transcriptomics, the ST dataset is again richer, because data points are anchored to a high-resolution image of the target tissue.

Our current AD research builds on previous strategies to identify gene expression changes that may identify novel markers or genes that can be targeted as biomarkers for interventions that halt or slow disease progression. We used male mice in an early phase of the disease and sought to identify key genes in either the hippocampus or OFBs to improve our understanding of the defects in synaptic transmission and odor sensing. We focused our analyses on three subsets of DE genes. First, we analyzed globally deregulated genes. Second, we identified significantly changed genes showing spatially restricted expression. Third, we defined genes that were significantly DE between 3xAD and 3xPB mice. Finally, we mined published data on these gene's expression in human AD brain tissue, to determine whether the results in mice translate to humans. One DE gene of interest is the gene encoding Bok. It was found to be specifically down-regulated in mouse AD brains. In addition, we provide validation that it is also deregulated in human Alzheimer brains via immunohistochemistry and publicly available single-nucleus RNA-seq data. This is, to our knowledge, one of the largest studies performed using ST, which has integrated both behavioral and molecular characterizations of two brain regions.

RESULTS

LTP and Olfaction in AD and Control Mice

In this study, we focused our molecular analyses on two regions of the mouse brain implicated in Alzheimer pathogenesis: the hippocampus and the OFBs from adult middle-aged male mice. We used male mice for a practical reason, as they perform better in smelling tests at this age. In addition, male mice show less pathology than females and we are interested in early gene expression changes before AD pathology is evident. Extensive ST analyses were performed with close to 50 tissue sections being analyzed with the transcriptome-wide *in situ* technology (three mice per genotype, and two sections per mouse). We used two inbred AD strains, namely, 3xAD (triple transgenic APP, PS1, and MAPT) and 3xPB (a quadrupole transgenic $\text{Pol}\beta^{+/-}$, APP, PS1, and MAPT), and two control mouse strains, namely, WT (wild-type C57BL/6J) and PB (transgenic $\text{Pol}\beta^{+/-}$). The AD models used here develop AD features much later than those of other AD mouse models and have been characterized previously (Hirata-Fukae et al., 2008; Hou et al., 2018; Liu et al., 2018; Misiak et al., 2017a; Sykora et al., 2015). In addition, behavioral changes are readily detected in our middle-aged mice (Hou et al., 2018; Misiak et al., 2017a; Sykora et al., 2015; www.alzforum.org/research-models).

We sought to evaluate mice in the early phase of the disease because we are interested in defining biomarkers of early disease. AD pathology was characterized by measures of inflammation (astrocytes or activated microglia) and patterns of A β deposition (intracellular or extracellular). The signal for astrocytes, marked by GFAP, was more abundant in 3xPB (Figure S1A). Astrocytes were mainly located in the hippocampus (Figure S1A), anterior olfactory nucleus, cortex, and cerebellum. In contrast, microglia, IBA-1 staining, were evenly distributed across the brains, but were like controls in morphology (Figure S1B). In both

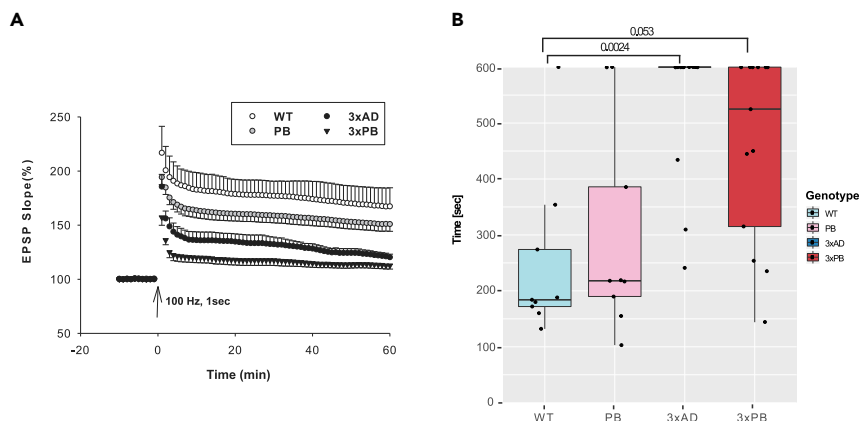


Figure 1. Application of ST to Understand Behavioral Changes in AD Mice

(A) Graphic representation of LTP results measured at the Schaffer collateral synapses. EPSP, excitatory postsynaptic potential. There were no differences in pre-synaptic transmissions. Six slices from a minimum of five mice per group were assessed, and the values represent the mean \pm SE.

(B) Graphic representation of results of the buried food test. Mice $n = 8$ –13 per genotype. Box plots hinges show 25th and 75 percentiles and sash mark shows median.

See also [Figure S1](#).

3xPB mice, there were a few $A\beta$ -positive extracellular deposits found (see arrows), but none were observed in the other mice ([Figure S1C](#)). Tau immunoreactivity was not assessed. Our results are consistent with similarly-aged mice described by Hirata-Fukae et al. ([Hirata-Fukae et al., 2008](#)), suggesting that the mice represent early aspects of AD pathology.

LTP measures synaptic transmission; is important for synaptic plasticity, memory, and learning; and is thought to be affected in AD. LTP specifically measures the ability of CA3 neurons to communicate with CA1 neurons via the Schaffer collateral synapses with modulation provided by the dentate gyrus (DG) ([Caruana et al., 2012](#)). Hippocampal LTP was significantly decreased in both AD strain mice ([Figure 1A](#)), down by 32.6% in 3xPB and 27.2% in 3xAD, relative to WT, as measured during the last 10 min of recording. PB mice also showed a significant decrease of 18.7% relative to WT mice. The significance of this finding is unknown but suggests that DNA repair is important for maintaining LTP.

As olfactory deficits are emerging as an early marker in AD neurodegeneration ([Murphy, 2019](#); [Rahayel et al., 2012](#)), we also measured olfactory function using a buried food test. The results showed that 3xAD and 3xPB mice performed less well than WT and PB mice, whereas PB and WT mice perform similarly in this assay ([Figure 1B](#)). We note that the average body weight of 3xAD and 3xPB mice is higher than the average body weight of PB and WT mice ([Figure S1D](#)). Although PB mice have mild deficits in LTP, relative to the AD strains, they performed like WT mice in the buried food pellet test.

These results are consistent with prior analyses of our mice, which typically used older animals ([Hou et al., 2018](#); [Misiak et al., 2017a](#); [Sykora et al., 2015](#)). This motivated us to explore the transcriptional landscape using molecular tools to identify genes within the hippocampal and olfactory neuronal layers that might contribute to these behavioral changes seen in our AD strains.

ST Identifies DE Genes and Molecular Clusters Corresponding to Anatomical Layers of the Mouse Hippocampus and OFB

In brief, snap frozen tissue samples from three animals of each genotype, were cryo-sectioned, stained, and imaged on barcoded glass surface. The tissue sections, two sections per mouse, were then cryo-sectioned, stained, and imaged on a barcoded glass surface. The tissue sections were then permeabilized to allow for mRNA to hybridize to the polyT-barcoded probes. The resulting cDNA products were released from the surface, after an on-chip reverse transcription step, and prepared for Illumina sequencing. ST libraries were generated from coronal sections of the hippocampus and OFB, and a total of 48 tissue sections were analyzed. This resulted in a total of 15,062 spots and 22,701 unique genes for the hippocampus

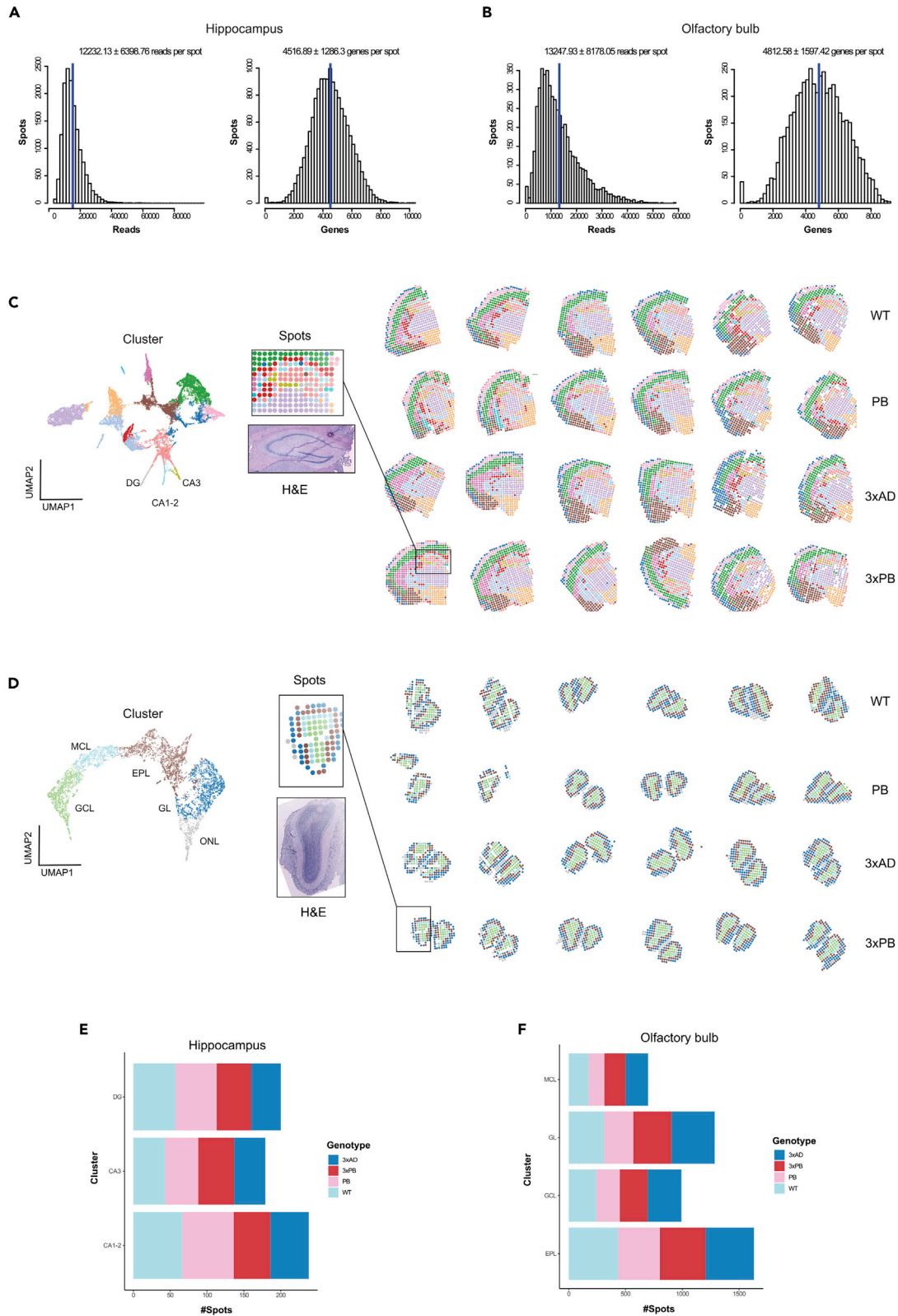


Figure 2. Statistics and Unsupervised Clustering Analysis

(A) Reads and genes per spot distributions for the hippocampus dataset (median \pm SD).

(B) Reads and genes per spot distributions for the OFB dataset (median \pm SD).

(C) Factor analysis of the hippocampus dataset. UMAP manifold of the factor activities colored by cluster and genotype on the left and clusters overlaid onto the tissue sections on the right.

(D) Factor analysis of the OFB dataset. UMAP manifold of the factor activities colored by cluster and genotype on the left and clusters overlaid onto the tissue sections on the right.

(E) Graphic representation of the number of spots per cluster per mouse genotype (hippocampus). Three mice per genotype and two slices per mouse were used.

(F) Graphic representation of the number of spots per cluster per mouse genotype (olfactory bulb). Three mice per genotype and two slices per mouse were used. See also [Figure S2](#).

dataset with an average of 12,232 reads and 4,516 genes per spot ([Figure 2A](#)). Similarly, we obtained 5,059 spots and 20,471 unique genes for the OFB dataset with an average of 13,247 reads and 4,812 genes per spot ([Figure 2B](#)). Unsupervised clustering of the spots belonging to the hippocampus dataset was performed using factor analysis, an approach that is designed to account for batch effects and other sources of technical variation ([Berglund et al., 2018](#); [Maaskola et al., 2018](#)). The annotation of the expression clusters was performed anatomically using the H&E images and the Allen Brain Atlas. This resulted in 14 well-defined gene expression clusters that correspond to the anatomical layers in the brain hemisphere ([Figure 2C](#)). We selected three clusters corresponding to hippocampal subfields CA1-2, CA3, and DG regions, well-known areas of pathological relevance for AD, for further analysis. Similarly, clustering analysis of the OFB dataset resulted in five well-defined clusters that clearly mapped the different layers of the OFB ([Figure 2D](#)). We selected the four clusters corresponding to the granular cell layer (GCL), mitral cell layers (MCL), the external plexiform layer (EPL), and glomerular layer (GL) for further analysis. The number of spots corresponding to the various clusters per genotype is shown in [Figures 2E](#) and [2F](#), while the breakdown of reads per spot is shown in [Figures S2A](#) and [S2B](#). In addition, UMAP manifolds of the factors displaying spots colored by genotype, animal, and chip show the lack of batch effects and the power of the factor analysis to capture the biological differences ([Figures S2C](#) and [S2D](#)).

We next performed multiple differential expression analyses. To identify DE genes, we conducted a genotype-based analysis where every genotype was compared with WT. Via those comparisons, we aimed to detect genes that are DE between the strains and control within each investigated cluster (i.e., proxy for individual anatomic regions). In a separate analysis, we aimed to detect genes that were DE between the clusters for each genotype, i.e., CA1-2 versus CA3. By this analysis, we sought to detect genes that have distinct spatial patterns. This resulted, after applying thresholds of log₂ fold-change 0.5 and adjusted p value 0.1, in 964 genes that are DE by genotype in the hippocampus ([Figure S3A](#)) and 993 genes that are DE by genotype in the OFB ([Figure S3C](#)). Venn diagrams depicting the overlap of the number of DE genes in the various anatomic regions are shown in [Figures S3B–S3D](#). We did not find any genes changing in the opposite direction between the hippocampus and OFBs. We also conducted a direct comparison between 3xAD and 3xPB to identify gene expression changes induced by loss of the DNA repair protein, Pol β ; a Venn diagram of that comparison is shown in [Figures S3E](#) and [S3F](#). Multi-volcano plots of all the DE genes ([Figures S4A](#) and [S5A](#)) and genes in our selected lists are shown in [Figures S4B](#) and [S5B](#).

Global Gene Expression Alterations in the Hippocampus and Olfactory Bulbs

Using ST data from the hippocampal and OFB regions, the results were then examined for gene(s) DE in multiple layers/clusters of each brain region in each strain. These we called the globally deregulated genes and constituted the DE genes from both datasets that were DE in more than a single layer (i.e., clusters). Very few genes were DE across every layer within any given genotype ([Figure S3 C-D](#)). These findings exemplify the importance of defining the individual DE gene sets for each layer and analyzing them separately. A total of 124 genes were DE in one or more layers in the hippocampus and OFB ([Figures 3A](#) and [3B](#)). The biological process gene ontology (GO) terms they fall into are shown in [Figure 3C](#). The enriched genes within the terms are shown in [Figure 3D](#). About one-third of the terms are related to metabolism, and another third are related to synaptic transmission and nervous system development. Response to reactive oxygen species, macroautophagy, and various kinase signaling terms were found within the remaining terms.

Only three genes were differentially regulated across both AD datasets but absent from PB gene lists: Ubiquitin C (*Ubc*) and *Gm10073* were downregulated in both AD strains, whereas Glyoxalase I (*Glo1*)

Figure 3. Identification of Genes Jointly Differentially Expressed in Hippocampi and Olfactory Bulb

(A) Venn diagram showing the numbers of statistically significant differentially expressed genes per region and the number of genes found in at least one region in both datasets.

(B) Heatmap showing the log₂ fold-change for the set of shared genes, 124 genes, in (A) hierarchically clustered by anatomic region.

(C) GO biological process terms enriched from genes shown in (B). Score represents statistical confidence, and ratio represents the relative number of genes detected in the term divided by all the input genes.

(D) Gene clustergram showing the overrepresented genes from the GO terms shown in (C). Score represents statistical confidence, and ratio represents the relative number of genes detected in the term divided by all the inputted genes.

See also [Figure S3](#).

was upregulated in both strains ([Figure 3B](#)). *Ubc* is a substrate for polyubiquitin reactions, which are integral to stress responses like DNA repair, innate immunity, proteome homeostasis, and the response to cellular stress. In this regard, UBC could promote dissolution of toxic protein aggregates, such as A β , a known issue in AD. In a recent large metadata analysis of human AD samples, *UBC* was identified as a key hub gene and downregulated in multiple brain regions ([Patel et al., 2019](#)), a result that is consistent with the present observations (e.g., downregulated in the hippocampus and OFB in AD but not PB mice). *Gm10073* is a pseudogene of unknown function that is strongly downregulated in the AD mice. *Glo1*, the only universally upregulated gene in both hippocampus and OFBs of AD mice, promotes detoxification of methylglyoxal, a toxic by-product of high glucose in cells, via the glyoxalase system ([Frandsen and Narayanasamy, 2018](#)). This system converts methylglyoxal to lactate using glutathione as a cofactor, blocking production of advanced glycation end products. Methylglyoxal is neutralized by GLO1 and GLO2 enzymes. Thus, these proteins help prevent proteins, lipids, and nucleic acids from being derivatized by methylglyoxal. Using mass spectrometry on the OFB tissue, several GLO1-interacting partners were found to be downregulated at the protein level: GRHPR, glyoxylate and hydroxypyruvate reductase; NDUFB10, NADH dehydrogenase and oxidoreductase; TALDO1, transaldolase of the pentose phosphate pathway that provides ribose-5-phosphate for nucleic acid synthesis and NADPH for lipid biosynthesis; and TPI1, which catalyzes the transfer of a hydrogen atom from carbon 1 to carbon 2 in an intramolecular oxidation-reduction reaction (see [Table S1](#) and Venn diagrams in [Figure S3G](#) for overlap between proteomics and transcriptomics).

To validate the increased expression of *Glo1* in the mice, we ran western blots of GLO1 and GLO2 to evaluate the whole pathway. Western blot analysis confirmed that the abundance of GLO1 is higher in AD mice than control mice; however, the abundance of GLO2 protein was lower, consistent with the notion that the glyoxalase system is severely deregulated in our AD strains ([Figure S6](#)). Notably, in humans, GLO1 protein was found to be upregulated in the early stages of human AD but downregulated in middle and late stages ([Kuhla et al., 2007](#)).

Identification of Spatially DE Genes in Hippocampus

The hippocampus plays a critical role in memory and learning. All the highly confident DE genes were subjected to biological GO term analysis and the top 25 enriched terms are shown in [Figure S7A](#), and a gene clustergram ([Figure S7B](#)) shows the overrepresented genes driving these term changes. There are multiple terms related to apoptosis and cell cycle, transcription, DNA metabolism (including DNA repair), and transforming growth factor β signaling. Protein degradation, deubiquitylation, and autophagy terms were also present. From the DE genes detected in the hippocampus dataset (964 genes, [Figure S3A](#)), we identified a list of 55 genes that showed significant differences in expression between genotypes and showed clear spatial patterns, a summary of these genes is provided in [Table S2](#). They were subjected to hierarchically clustered (by rows) heatmaps of normalized expression ([Figure 4A](#)), log₂-fold-change ([Figure 4B](#)), and individual gene plot (normalized gene expression plotted onto the tissue sections) analyses ([Figure 4C](#)).

Several genes were DE across all hippocampal layers. Protein kinase muscle (*Pkm*), cytochrome c oxidase subunit 6c (*Cox6c*), ribosomal protein S2 (*Rps2*), and transmembrane 59 like (*Tmem59l*) were downregulated in the AD strains ([Figures 4A](#) and [4B](#)). Two of these genes, *Pkm* and *Cox6c*, are important in glycolysis and respiration, respectively. *Tmem59l* plays a role in autophagy, which is a general stress response to starvation, growth factor deprivation, and endoplasmic reticulum (ER) stress. Downregulation of *Tmem59l* has been shown to prevent caspase-dependent neuronal cell death ([Zheng et al., 2017](#)). Based on its sequence similarity to *Tmem59*, it may directly regulate APP processing and A β localization ([Ullrich et al., 2010](#)). The upregulated genes were gamma-aminobutyric acid (GABA) receptor subunit alpha-2 (*Gabra2*), Lipoprotein lipase (*Lpl*) and WW domain-binding protein 11 (*Wbp11*). *Gabra2* encodes a subunit of the chloride channel and receptor for the major neuroinhibitory transmitter GABA. *Lpl* protein is a triglyceride hydrolase that

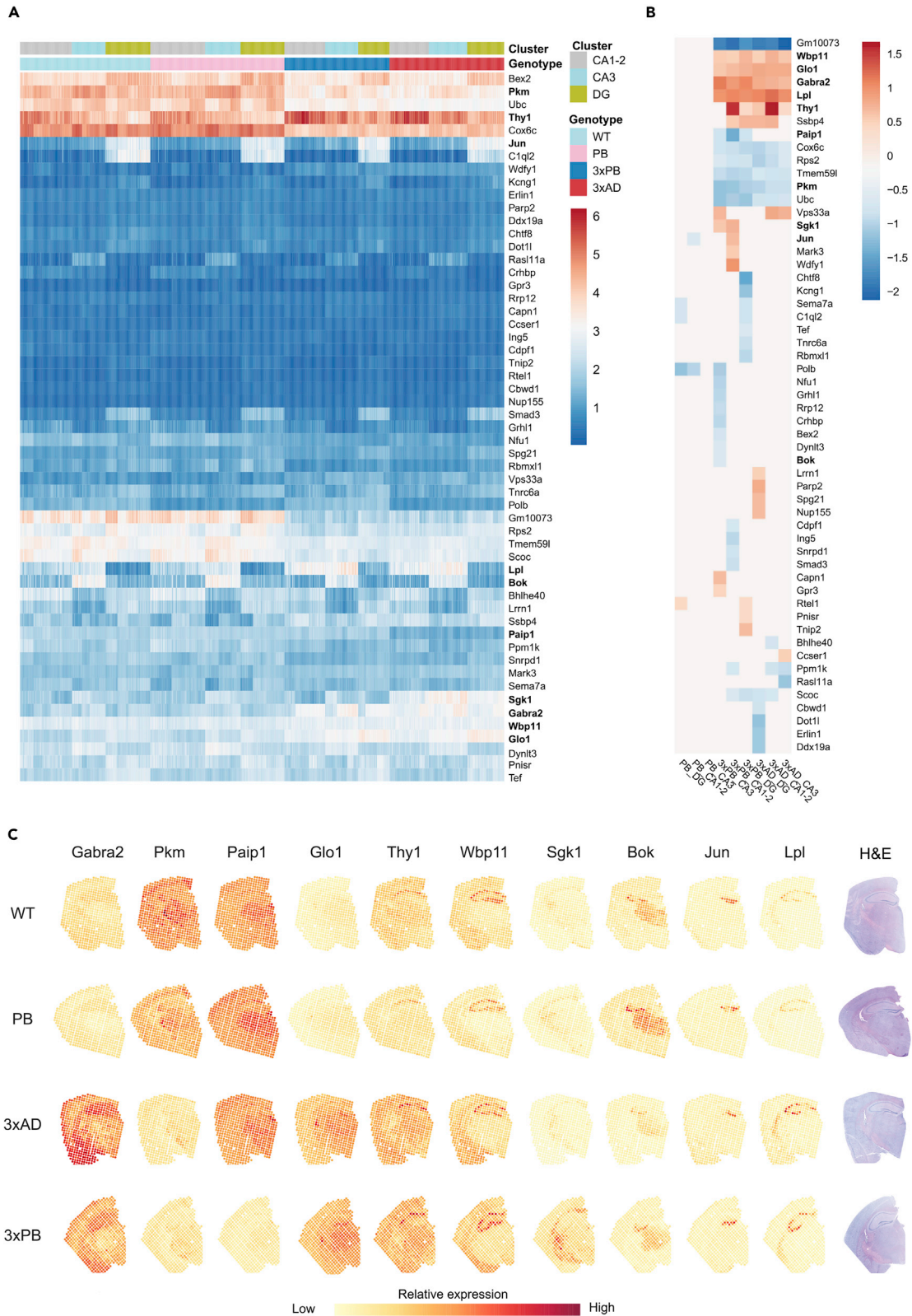


Figure 4. ST Analysis on Hippocampi Regions Reveals Differences among Stress Response Signaling Genes Globally and Regionally

(A) Heatmap of the spatially differentially expressed genes found in the hippocampi clustered by rows. Graphic colored by normalized expression and separated by color-coded genotype and cluster region.

(B) Heatmap of log₂-fold-change values of genes shown in (A) clustered by rows and columns.

(C) Graphic representation of normalized gene expression of selected genes overlaid onto brain sections. The genes represent the types of data seen.

Shown are *Gabra2*, *Pkm*, *Paip1*, *Glo1*, *Thy1*, *Wbp1*, *Sgk1*, *Bok*, *Jun*, and *Lpl*. H&E-stained brain slices are shown on the right.

See also [Figures S4](#) and [S6–S9](#).

facilitates lipid uptake, including A β uptake, to promote its degradation (Nishitsuji et al., 2011). Importantly, it is also described as a microglia disease-associated marker (Keren-Shaul et al., 2017). *Wbp11* encodes a splicing factor (Llorian et al., 2004), and its expression was significantly upregulated throughout the brain hemisphere. Representative gene expression plots for some of the genes can be seen in [Figure 4C](#), and representative full gene plots for several of these genes are shown in [Figure S8](#). As can be seen some genes show greater variability between mice than others, notably *Gabra2* and *Cox6c*.

To identify genes that display spatially restricted expression, we evaluated the heatmaps ([Figures 4A](#) and [4B](#)) and the gene plots, which shows a gene's normalized expression values overlaid onto the tissue sections ([Figure 4C](#)). Several genes stood out by this analysis. Although *Lpl* was upregulated across all AD-associated clusters of the hippocampus ([Figures 4A](#) and [4B](#)), it was visibly upregulated in the CA1-2 and CA3 sublayers of the hippocampus ([Figures 4C](#) and [S8](#)). We have previously demonstrated *Lpl* protein upregulation by western blotting and suggested that it may contribute to altered fat metabolism in our mice (Demarest et al., 2020). *Thy1* was also upregulated in the AD strains' CA1 regions and throughout the brain hemisphere. Here, it should be noted that the *Thy1* promoter drives expression of the AD transgenes. Two genes, Bcl-2-related ovarian killer (*Bok*) and Ras-like family 11 member A (*Rasl11a*), displayed decreased expression in the CA3 and thalamus regions (via inspection of images) ([Figures 4C](#) and [S8](#)). BOK is a multifunctional BCL2 family member protein that participates in the intrinsic mitochondrial pathway of apoptosis, and there are reports of BOK as a pro-apoptotic (Llambi et al., 2016) agent or not (D'Orsi et al., 2016). Interestingly, BOK may also be important for calcium homeostasis, mitochondrial dynamics, and bioenergetics (D'Orsi et al., 2016; Schulman et al., 2019). *Rasl11a* protein has been reported to enhance rDNA transcription via RNA polymerase I, and its downregulation here may impinge upon the assembly of rRNA components and translation specifically in the CA3 and thalamus regions ([Figure S8](#)). RNAscope was used to validate the localized expression changes of *Gabra2*, *Bok*, and *Lpl* ([Figure S9](#)).

The AP-1 transcription factor subunit and immediate-early gene, *Jun*, is an illustrative example of the power of spatially resolved gene expression analysis ([Figures 4](#) and [S8](#)). *Jun* is a DE gene; however, *Jun* was visibly expressed in the DG of the AD strains ([Figures 4C](#) and [S8](#)) but was only DE in the CA1 of 3xPB mice ([Figure 4B](#)). Thus, we chose not to focus further attention on genes that display this type of expression pattern.

Genes Important in Translation and Stress Response Signaling Are Revealed in the Comparison of 3xAD and 3xPB Mice

At the outset of this project, we sought to gain insights into the differences between 3xAD and 3xPB mice because disease progression is faster in the DNA repair-deficient 3xPB mice (Hou et al., 2018; Misiak et al., 2017a; Sykora et al., 2015). A DE analysis was performed to directly compare 3xAD and 3xPB mice using all layers; Venn diagrams of the genes that overlap are shown in [Figures S3E](#) and [S3F](#). Fewer genes were DE between these two strains than between either of them compared with WT mice. This is to be expected, as they are highly inbred. There were 144 highly confident DE genes in the hippocampus and 198 genes in the OFBs 3xPB ([Figures S3E](#) and [S3F](#)). The hippocampal genes that stood out by this analysis included *Paip1*, *Eif3f*, *Sgk1*, *Rpa2*, *Gadd45a*, *Cdkn1a*, and of course *Polb*. In the hippocampus, the Poly(A) binding protein interacting protein 1, *Paip1*, was globally downregulated in 3xPB mice, but not in 3xAD mice. The protein encoded by this gene participates in translation initiation, and elements of LTP require nascent translation (Johnstone and Raymond, 2013). The gene *Eif3f* is also involved in translation regulation (Shi et al., 2006). The serum glucocorticoid-regulated kinase 1, *Sgk1*, was uniquely upregulated in 3xPB mice, visibly in the fornix, which is the major output track from the hippocampus. *Sgk1* is a major stress response kinase and one of a few genes deregulated in both the hippocampus and OFBs in the 3xPB mice ([Figure 3B](#)). It participates in several stress-associated signaling cascades including NF- κ B and GSK3 β -PPAR α signaling (Lang et al., 2018). RPA2, GADD45A, CDKN1a (p21) and POL β proteins are all important in the response to DNA damage, and this finding is consistent with our previous report that our 3xPB mice accumulate more DNA damage (Sykora et al., 2015).

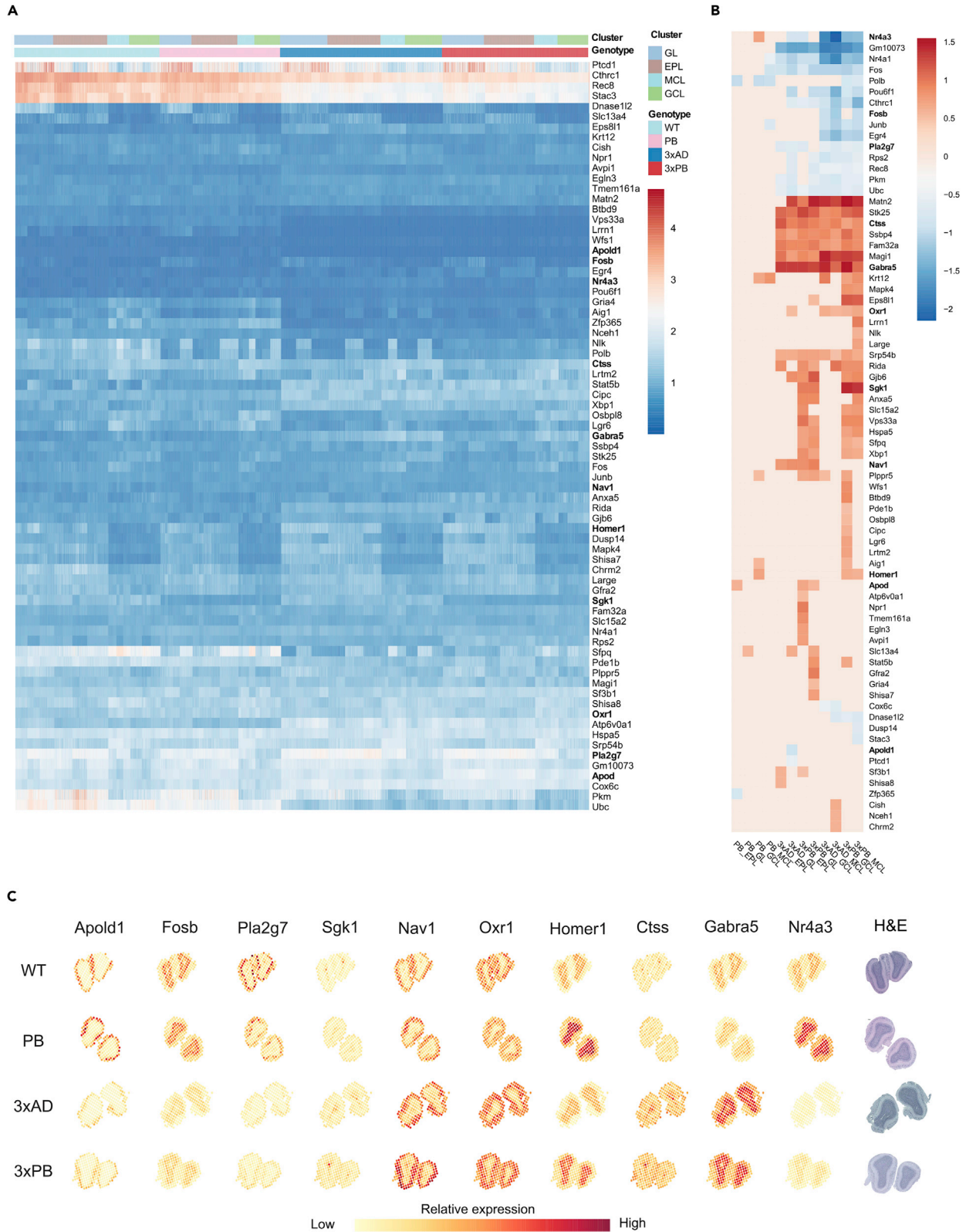


Figure 5. ST Analysis on Olfactory Bulbs Reveals Differences among Synaptic and Stress Response Signaling Genes both Globally and Regionally

(A) Heatmap of the differentially expressed genes found in the OFBs clustered by rows. Graphic colored by normalized expression and separated by color-coded genotype and cluster region.

(B) Heatmap of log₂-fold-change values of genes shown in (A) clustered by rows and columns.

(C) Graphic representation of normalized gene expression of selected genes overlaid onto olfactory bulb tissue sections. Genes changed by region include *Apo1d1*, *Fosb*, *Pla2g7*, *Sgk1*, *Nav1*, *Oxr1*, *Homer1*, *Ctss*, *Gabra5*, and *Nr4a3*. H&E-stained brain slices are shown on the right. See also [Figures S5](#), [S10](#), and [S11](#).

Identification of Spatially DE Genes in Olfactory Bulbs

Olfactory function is emerging as an important early marker for neurodegeneration and AD ([Murphy, 2019](#); [Rahayel et al., 2012](#)). AD mice suffer from a variety of progressive olfactory deficits; however, we do not have good biomarkers for AD olfactory dysfunction. All the OFB DE genes were subjected to biological GO analysis, and the top 25 enriched terms are shown in [Figure S9A](#) with the genes overrepresented in these terms shown in [Figure S9B](#). Notably, there were multiple terms for transcription, ion transport including chemical synaptic transmission, TGF β signaling, and programmed cell death. Using the same analysis strategy as discussed above for the hippocampus, we identified 73 DE genes that displayed spatial expression in the OFBs ([Figures 5A](#) and [5B](#)). A summary of the genes discussed below is shown in [Table S3](#).

Most of the globally downregulated genes were shared with the hippocampus, except for phospholipase A2 group 7, *Pla2g7*. This protein is involved in the breakdown of oxidized phospholipids and is known to suppress mitochondrial apoptosis ([Chen et al., 2007](#)). In WT and PB mice, *Pla2g7* showed marked expression in the outer layers of the OFBs, and this was lost in the AD strains ([Figure 5C](#)). Validation of some of the globally deregulated OFB genes was confirmed by mass spectrometric analysis ([Table S1](#)).

One POU family transcription factor, *Pou6f1*, was found to be significantly downregulated throughout the OFBs of the AD strains. OFB interneurons secrete the neuropeptide corticotropin-releasing hormone (CRH), which promotes synaptic plasticity in the OFB. The receptor for CRH, CRHR1, activates CREB-dependent transcription. *Pou6f1* has a CREB-binding site in its promoter and loss of POU6F1 protein in CRHR1+ neurons causes reduced synaptic connectivity and dendritic complexity, whereas overexpression of POU6F1 induces dendrite outgrowth, branching, and synapse plasticity ([McClard et al., 2018](#)). Our results suggest that diminished expression of *Pou6f1* in both the OFBs and hippocampus may substantially alter synaptic functionality and contribute to loss of the sense of smelling and LTP, in the AD strains. Interestingly, Blalock et al. demonstrated that *Pou6f1* was downregulated in patients with incipient AD via microarray of hippocampal tissue ([Blalock et al., 2004](#)).

There are clear indications of stress across the OFBs. We detect upregulation of *Glo1*, discussed earlier, oxidant-stress response kinase (*Stk25*), cathepsin S (*Ctss*), and *Fam32a* globally ([Figure 5B](#)). STK25 is a kinase and Golgi protein that regulates Golgi morphology and cell death, in part by its translocation from the Golgi to the nucleus in response to stress. It plays roles in lipid metabolism, glycolysis, and glucose and insulin homeostasis. CTSS is a cysteine protease thought to contribute to autophagy, the degradation of proteins and organelles for self-protection. *Fam32a* and *Srp54b* are globally upregulated splicing factors. A recent proteomic study using brains of patients with AD patient deduced that many AD proteins are subjected to RNA splicing and that the alternatively spliced proteins correlate with AD pathology and cognition ([Johnson et al., 2018](#)). Another gene globally deregulated in the OFBs was *Gabra5* ([Figures 5B](#), [5C](#), and [S10](#)). It is a subunit of the GABA A receptor and was significantly upregulated across the AD OFBs but with greater expression in the GCL layer. Representative examples of the OFB globally deregulated gene expression patterns we saw are exemplified by *Cox6c* and *Fam32a* ([Figure S10](#)).

Proteomic analysis on the OFBs revealed 859 DE proteins, of which 20 were changed in opposite directions between the AD strains. None of the genes encoding these proteins were represented in our ST dataset. All DE proteins were subjected to GO-BP analysis; see [Table S4](#) for the significant terms. Among the top 25 terms, RNA splicing (six terms) was overrepresented. The top term, plus two additional from the list of top 25 terms, was associated with mitochondrial electron transport. The single neuronal item, among these top terms, was associated with neuron projection development. See [Table S4](#) for the full list of significant GO-BP terms. There were 92 proteins/genes that were shared between the proteomics and transcriptomics analyses. Up- and downregulated proteins were similar between the AD strains. Of the genes we discuss here, the direction of change for PKM, COX6C, and MAG11 were consistent between the two types of

analysis, whereas Nav1 and HSPA5 were not. The joint list of proteins/genes (Table S1) was subjected to GO-BP analysis. Among the top 25 terms, terms relating to cytoskeleton and actin organization (six terms), glycolysis (three terms), and antigen processing (three terms) were overrepresented. Four terms were related to neuronal function including generation and differentiation of neurons, synaptic transmission, and long-term synaptic potentiation. See Table S5 for the full list of GO-BP terms.

Notably, by mass spectrometric analysis, APOE was highly overexpressed, particularly in the OFB of 3xPB mice (Table S1). APOE is a lipoprotein, and one of its alleles, ApoE4, is found in 65% to 80% of patients with late-onset AD, reviewed in Misiak et al. (2017b). ApoE, by ST analysis, showed minor upregulation in the GL and EPL of AD OFBs. *Apod*, however, was upregulated in a few layers (Figure 5B). THY1 and MTOR (both downregulated) and MTOR-interacting proteins, AKT1S1 and LAMTOR2 (both upregulated), were deregulated in the mass spectrometric analysis (Table S1).

Olfaction is unaffected in PB mice. Therefore, we postulated that we might gain insight into the mechanism of olfactory dysfunction in AD, by identifying genes that are DE in the OFB of 3xAD and 3xPB mice, but not in PB mice. The AD strains had increased expression of oxidation resistance 1 (*Oxr1*), natriuretic peptide receptor 1 (*Npr1*), and neuron navigator 1 (*Nav1*). In contrast, expression of Apolipoprotein L domain containing 1 (*Apold1*) was lower in the outer layers of the OFBs (Figures 5B and 5C). Mice lacking *Oxr1* display neurodegeneration, and point mutations in this protein contribute to epilepsy in humans (Oliver et al., 2011). In yeast and human cells, OXR1 is localized to mitochondria, where it protects them from oxidative stress. NAV1 associates with the growth cones and branch points of microtubules and is thought to be involved in axon guidance and synaptic maturation (Martinez-Lopez et al., 2005). *Nav1* is upregulated in 3xPB mice EPL and GL. Overexpression of mouse NAV1 in cultured neurons leads to rearrangement of microtubules into bundles. NPR1 is a membrane bound guanylate cyclase that binds natriuretic peptides, which promote vasodilation (Pandey, 2018). *Apold1* was downregulated in the GL, and this gene plays roles in endothelial cell signaling, vascular injury, and cellular permeability (Regard et al., 2004). Several of the genes discussed are shown in Figures 5A and 5B, their relative spatial expression patterns are shown in Figure 5C, and their full gene plot is shown in Figure S10.

Several immediate-early genes were downregulated in the AD strains: *Fosb*, *Fos*, *Junb*, *Egr4*, *Nr4a1*, and *Nr4a3*. The intermediate-early genes regulate transcription, synaptic plasticity, and intracellular signaling. Notably, *Fosb* and *Nr4a3* showed clear expression in the MCL and GCL of WT and PB mice OFBs, whereas they were significantly downregulated in the AD strains' samples (Figures 5C and S10). *Fosb* is an alternatively spliced gene used as a marker for neuronal activity and is important for stress responses in the brain (Hiroi et al., 1997). NR4A3 functions in many pathways including neuronal differentiation, apoptosis, metabolism, and cell cycle progression (Paillasse and de Medina, 2015). In beta cells, knockdown of this gene reduced mitochondrial respiration in permeabilized cells (Reynolds et al., 2016). Some of these genes, *Fos*, *Nr4a1*, and *Junb*, were also downregulated in PB mice, so it is unclear if these genes contribute to the olfactory deficits in the AD strains because PB mice do not display smelling defects.

In WT mice, *Polβ* was found to be expressed throughout the OFBs (Figure S10) and *Homer1* showed significant upregulation in the MCL and GCL in a *Polβ*-dependent manner. HOMER1 is a postsynaptic density scaffolding protein that regulates metabotropic glutamate receptor function and calcium release (Jardin et al., 2013). *Homer1* displayed a clear spatial upregulation in the GCL and MCL (Figure 5C). Currently, it is unclear how or why loss of *Polβ* promotes increased expression of *Homer1* or its functional consequences. We should note here that *Paip1* and *Homer1* genes are both located on mouse chromosome 13, whereas the *Polβ* gene is located on mouse chromosome 8. So, their change in expression is not due to a direct interaction with the inactivation of the *Polβ* gene. Obviously, we cannot rule out some off-target integration events or higher-order chromatin interactions.

As done earlier in the article, biological process GO terms linked to genes DE in the OFB of 3xAD and 3xPB mice were tabulated and analyzed. The most highly enriched GO terms were stress response signaling and lipid metabolism. *Sgk1* and *Xbp1* are among the few genes deregulated in both the OFBs and hippocampus (Figure 3B). *Sgk1* was upregulated globally in 3xPB mice, but with a distinct pattern in the center of the OFB GCL (Figures 5C and S10). *Xbp1* was globally upregulated across the OFBs of 3xPB mice (Figure S10). It is a multifunctional transcription factor that functions in the immune system, lipid metabolism, and ER stress response (Cisse et al., 2017).

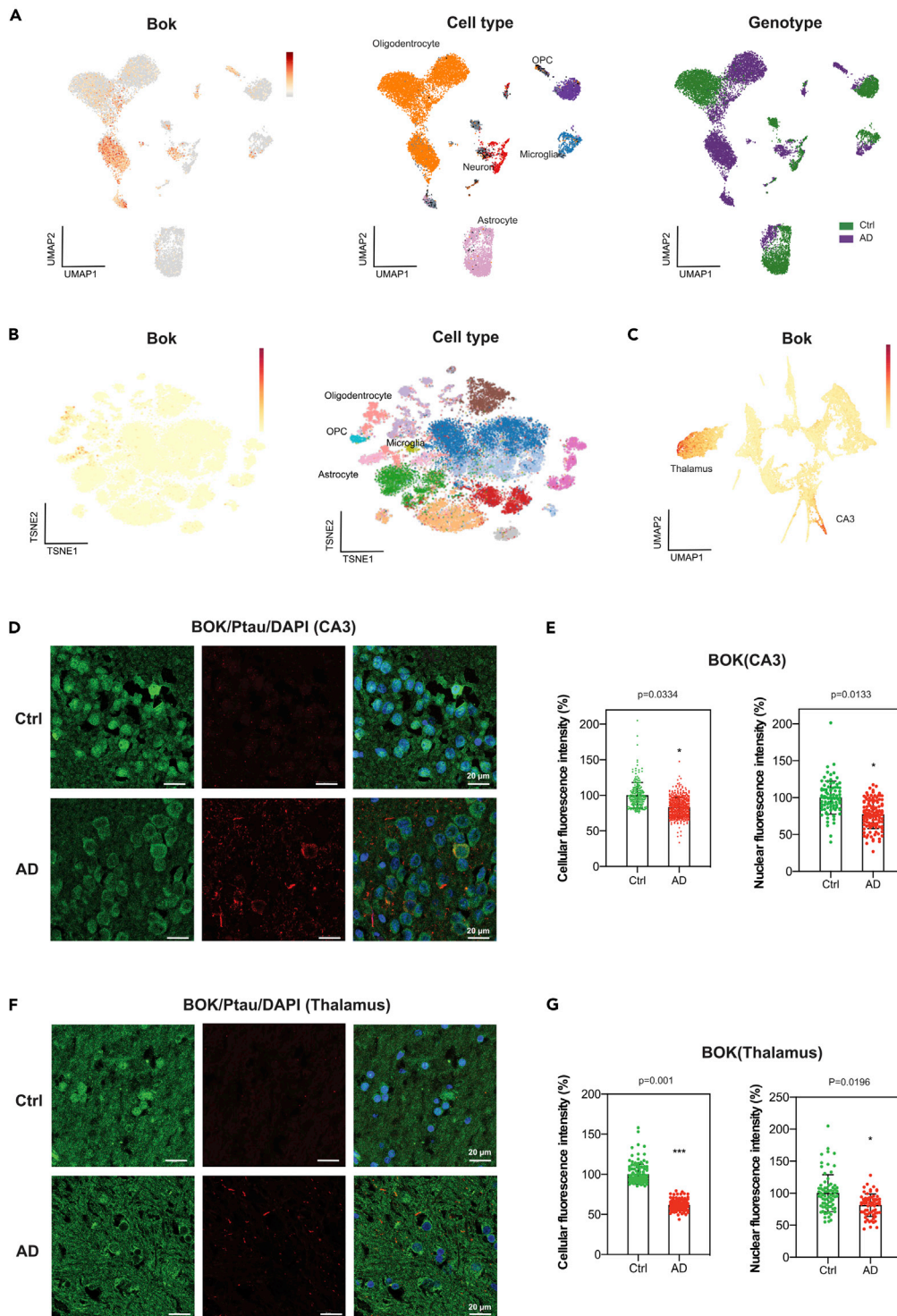


Figure 6. BOK Is Differentially Expressed in Human and Mouse AD Brains

(A) Single-nuclei RNA-seq generated from the entorhinal cortex of human AD and control postmortem brains (data from Grubman et al., 2019). UMAP manifold of single nuclei colored by BOK's normalized expression (red means higher expression level) together with genotype and cell type maps.

(B) Single-nuclei RNA-seq generated from the parietal lobe of human AD. t-SNE manifold of single nuclei colored by BOK (normalized expression) together with cell types. Data from Del-Aguila et al. (2019).

Figure 6. Continued

(C) UMAP manifold of factor activities colored by *Bok*'s normalized expression. The manifold is the same as in Figure 2C. The regions corresponding to the thalamus and CA3 are labeled. Localization of *Bok* denoted with red dots.

(D) Alteration of BOK protein level and localization in AD hippocampi. Representative images of coronal CA3 sections from human control (Ctrl) and Alzheimer (AD, Braak VI) hippocampi. Scale bars, 20 μ m.

(E) Quantification of images of BOK staining in hippocampi. The cellular and nuclear BOK fluorescence intensities were quantified within CA2/CA3 cells from Ctrl and AD hippocampi (cellular Ctrl, n = 237; AD, n = 493) (nuclear Ctrl, n = 86; AD, n = 115). Data are presented as mean \pm SEM. Statistical significance was determined using per brain mean value; three brains per category were analyzed.

(F) Alteration of BOK protein levels and localization in AD thalami. Representative images of coronal sections from human control (Ctrl) and Alzheimer (AD, Braak VI) thalami. Scale bars, 20 μ m.

(G) Quantification of images of BOK staining in thalami. The cellular and nuclear BOK fluorescence intensities were quantified within cells from Ctrl and AD thalami (cellular Ctrl, n = 127; AD, n = 133) (nuclear Ctrl, n = 74; AD, n = 67). Data are presented as mean \pm SEM. Statistical significance was determined using per brain mean value; three brains per category were quantified.

BOK, a Spatially Expressed Gene in Hippocampal CA3 Regions, Shows Loss of Expression in Mouse and Human AD Brains

Dysfunctional mitochondria contribute to AD pathology (Swerdlow, 2018). BOK is a mitochondrial protein that participates in mitochondrial apoptosis (D'Orsi et al., 2017; Einsele-Scholz et al., 2016) and mitochondrial dynamics (Schulman et al., 2019). Based on our ST data presented earlier, *Bok* is also downregulated in the hippocampus CA3 region and thalamus in 3xAD and 3xPB mice (Figures 4, 4C, and S8). This suggests the possibility that BOK could play a role in AD pathology. To determine if any of our DE genes, which also showed spatially restricted expression, were DE in human AD datasets, we obtained a human single-nuclei RNA-seq dataset composed of AD and healthy entorhinal cortex samples and probed for our genes (Grubman et al., 2019). UMAP plots of human AD BOK expression from this dataset are shown in Figure 6A. A subset of AD oligodendrocytes and cells of mixed origin appeared to upregulate BOK. BOK expression was also found altered in oligodendrocytes (upregulated) and neurons (downregulated) from parietal lobe tissue in another human single-nuclei RNA-seq AD dataset (Del-Aguila et al., 2019) (Figure 6B). In our datasets, we cannot distinguish the cell types of origin, but we find decreased expression of *Bok* in the CA3 region of the hippocampus and thalamus in 3xAD and 3xPB mice (Figures 4, S8, and 6C). Presumably, genes that display distinct layer-specific expression serve a specialized function in that tissue layer and thus, their DE in those layers, may impact cell biology to a greater extent. To evaluate BOK in human AD pathology, we performed BOK immunofluorescence labeling in hippocampal and thalamic brain sections from postmortem AD patients and non-demented controls. In both regions, there was a clear diminution of total cellular fluorescence signal for BOK, and this was largely driven by loss of nuclear BOK signal (Figures 6D–6G). These results are consistent with our observation of decreased hippocampal and thalamic BOK in our AD mouse models. An analysis of the biological implications of BOK loss is beyond the scope of this article.

DISCUSSION

ST is an emerging technology that pairs quantitative transcriptomics with high-resolution tissue imaging and unbiased bioinformatic analyses, anchoring the expression data to the physical map of the organ or tissue(s) of interest. This type of analysis facilitates molecular characterization of tissue sections and cellular layers in an unbiased fashion. Here, we applied ST to chart gene expression in the hippocampus and OFBs of 3xAD, 3xPB, PB, and WT mice. We identify differential expression of novel and known genes in AD mouse brain and confirm spatially restricted differential expression of BOK in the brains of human patients with AD.

Genes that were globally deregulated may have profound and systemic implications, i.e., *Ubc*, *Pkm*, *Cox6c*, and *Glo1*, because all these genes can impact the metabolic state of the cell. As UBC protein is a substrate for polyubiquitin reactions, decreasing it may contribute to impaired proteasomal degradation and DNA repair while promoting inflammation and the accumulation of misfolded A β or tau. As mentioned earlier in the article, it has already been reported that UBC is a key hub gene and downregulated in multiple human AD brain regions (Patel et al., 2019). Downregulation of *Pkm*, which plays a role in glycolysis, and *Cox6c*, which functions in Complex IV of the electron transport chain, both have the potential to directly contribute to loss of ATP generation and to the glucose hypometabolism seen in patients with AD (Mosconi et al., 2008). There is a high demand for energy during synaptic transmissions (Liotta et al., 2012), thus any deviation from optimum energy production may impact neuronal function.

Glo1 is a part of the methylglyoxal detoxification pathway, and increased expression here likely reflects the stress response to AD pathology. Interestingly, methylglyoxal, and the advanced glycation end products it produces, are elevated in patients with AD and may contribute to accumulation of insoluble A β - and APOE-dependent pathologies (Angeloni et al., 2014). With respect to LTP or smelling, derivatization of proteins by methylglyoxal could interfere with the dynamics of protein complex assemblies and thereby interfere with these functions. Furthermore, glutathione is used as co-substrate for methylglyoxal detoxification and deregulation of this pathway likely contributes to the depletion of glutathione, an important cellular antioxidant.

ST analysis also revealed that *Gabra2* is upregulated across the hippocampus, whereas *Gabra5* is upregulated in the OFBs in the AD strains. GABAergic synapses are critically important for the excitatory and inhibitory balance in the brain. There are 16 GABRA subunits, which form pentameric channels. Overexpression of *Gabra2* modulates postsynaptic currents by its increased GABA affinity, which causes slower current deactivation (Dixon et al., 2014). *Gabra5* is the main GABA A receptor responsible for tonic inhibition in the hippocampus (Glykys and Mody, 2006). It has been reported to be significantly downregulated in the CA1 area of human AD brain samples (age range of patient with AD: 75–85) (Rissman et al., 2007). GABA signaling also modulates neuronal homeostasis, adult neurogenesis, and neuroblast migration. Both proteins are known to regulate dendrite outgrowth and spine maturation. Overexpression of either subunit in their respective regions may modulate LTP in the hippocampus and synaptic transmission in the OFBs. Deregulation of these genes may contribute to AD pathology or be a compensatory response to AD pathology; further research is needed to clarify.

Our focus on genes that displayed spatially restricted expression patterns was an attempt to identify novel genes that may be linked to deficits in the specialized cellular layers of the hippocampus and OFBs in the AD strains. Among the spatially resolved genes that we identified, the pathways that these genes are associated with are highly cited as important in AD including lipid metabolism (*Lpl*, *Pla2g7*, *Apo1d1*), stress response genes (*Glo1*, *Sgk1*, *Bok*, *Oxr1*, *Stk25*, *Ctss*), and immediate-early genes (*Fosb*, *Nr4a3*). It is worth noting that deregulation of lipid metabolism genes in the outer layers of the OFB, GL, and EPL may alter odor information processing that is projected from the olfactory receptor neurons in the nasal cavity to the OFBs. ApoE protein is also expressed in these regions, and there is a clear association between ApoE4 and olfactory dysfunction in AD (Misiak et al., 2017b).

As mentioned earlier, the ST data presented showed spatially restricted DE of *Bok* in the hippocampus of AD mice. We propose that expression of *Bok* is relevant to AD, because of the strong association between mitochondrial dysfunction and AD and the established mitochondrial functions of BOK. Furthermore, our analyses confirm differential expression of *BOK* in brains of human patients with AD (Del-Aguila et al., 2019; Grubman et al., 2019). Our earlier analyses using microarray technology also suggested differential expression of *Bok* in AD mice (Hou et al., 2018), but without the added spatial context provided by the ST analysis it was not pursued. BOK protein has a variety of functions. It has been reported to regulate mitochondrial morphology (Schulman et al., 2019) and nucleotide metabolism (Srivastava et al., 2019) and suppress poly ADP-ribose polymerase-dependent cell death (D'Orsi et al., 2016). It can also function as a primary regulator of mitochondrial outer membrane permeabilization, an essential event in mitochondrial apoptosis (Llambi et al., 2016). BOK can trigger mitochondrial outer membrane permeabilization in the absence of other BCL-2 members, after inhibition of the proteasome (Zheng et al., 2018). Importantly, each of these factors may contribute to neuronal degeneration (Desler et al., 2017; Fang et al., 2019; Kam et al., 2018). In addition, hippocampal pyramidal neurons in the CA1 and CA3 display differential vulnerability to neuronal injury (Mattson et al., 1989), and *Bok*'s preferential expression in CA3 may contribute to this phenomenon. Neuronal cell death in either the hippocampus or OFB could impede performance in function. In mouse and human AD brains, *BOK* showed decreased expression in the hippocampus and thalamus (Figures 4 and 6). Notably, in human AD, we saw that BOK protein was mainly decreased in the cell nuclei, and high levels of nuclear BOK have been associated with induced apoptosis (Bartholomeusz et al., 2006). Thus, we speculate that decreased nuclear BOK may be a compensatory response to prevent cell death in response to AD pathology. Importantly, the role of mitochondria in AD pathology is still emerging, and BOK may contribute to the mitochondrial AD stress response. Additional analyses will be necessary to determine more precisely BOK's role in responding to AD-associated pathology.

Our working hypothesis is that loss of DNA repair changes the rate of disease progression, and consistent with this, we typically find that 3xPB mice display more progressive AD features than 3xAD mice (Hou et al., 2018; Misiak et al., 2017a; Sykora et al., 2015). Thus, here we sought to compare the DE genes between 3xAD and 3xPB to identify candidate genes that might contribute to this phenomenon. In the hippocampus, we find genes important in translation, *Paip1* and *Eif3f*, and stress and DNA damage response genes, *Sgk1*, *Rpa2*, *Gadd45a*, and *Cdkn1a*. LTP is one of the main mechanisms that facilitates acquisition, storage, and retrieval of information from neuronal circuits (Dringenberg, 2020). It is known that late LTP requires protein translation, and therefore loss of expression of translation genes in 3xPB may contribute to their diminished memory retention (Sykora et al., 2015). In the OFBs, *Sgk1*, *Xbp1*, *Homer1*, *Mtor*, and *ApoE* may all contribute to the differences between 3xPB and 3xAD. The alteration in the stress and DNA damage responsive genes are likely compensatory responses to loss of Pol β and expression of the AD transgenes. The energetic demands of responding to DNA damage may decrease the availability of ATP thereby slowing or delaying signal transduction cascades, increasing the presence of senescent cells, and contributing to the death of neurons. All these factors likely contribute to the behavioral changes between 3xPB and 3xAD mice. Moving forward, it will be important for us to evaluate the temporal deregulation of these genes and determine how their expression correlates with AD pathology and behavioral changes.

AD is a complex, multifactorial, progressive disorder. Here, ST was used to identify novel and known genes that may contribute to disease pathology or that contribute to the response to AD pathology. The DE genes may represent a pool of potential biomarkers for early AD. What is known about mitochondrial involvement in AD pathology is an expanding area of research, and this work identifies many genes that impinge upon mitochondrial functions. Although many of the genes we identified here were already known to be dysregulated in AD pathology, we identify BOK as a novel downregulated gene in both mice and human hippocampus and thalamus AD samples.

Limitations of the Study

Although ST is a powerful technology, we note the following limitations of the current study: (1) we are not able to ascribe any gene changes to a particular cell type in part because any given spot can contain multiple cells, (2) the tissue slices we analyzed did not encompass any anatomic region entirely, and (3) we have not identified the biological significance of any of the gene changes observed. In addition, as the OFB and hippocampus analyses were conducted on two separate cohorts of mice, of slightly different age, we cannot exclude that some of the gene changes are due to aging.

During the preparation of this manuscript, other techniques like Slide-seq (Rodrigues et al., 2019) and 10X Visium and image-based techniques like SeqFISH, MERFISH, and STARmap have been developed that may yield similar results (Burgess, 2019). In addition, high-definition ST (Vickovic et al., 2019) is another technique, but with lower throughput.

Resource Availability

Lead Contact

Vilhelm A. Bohr (vbohr@nih.gov)

Materials Availability

No new materials were generated in this article.

Data and Code Availability

Processed and analyzed data and analysis scripts generated during this study are available at Mendeley <https://doi.org/10.17632/6s959w2zyr.1> and GitHub https://github.com/jfnavarro/AD_POLB_ST. The mass spectrometry proteomics data have been deposited to the ProteomeXchange Consortium via the PRIDE (PubMed ID: 30395289) partner repositories with the dataset identifier PXD017766.

METHODS

All methods can be found in the accompanying [Transparent Methods supplemental file](#).

SUPPLEMENTAL INFORMATION

Supplemental Information can be found online at <https://doi.org/10.1016/j.isci.2020.101556>.

ACKNOWLEDGMENTS

We would like to thank Jane Tian, and Drs. Magda Misiak, Yujun Hou, and Tyler Demarest for their help with tissue collection; Eduardo Zavala for help with western blotting; Dr. Yang Heng and Prof. Erik Boddeke for assistance with immunohistochemistry; and Reza Mirzazadeh for help. We thank Drs. Yujun Hou and Kala Puligilla for critically reading the manuscript and their comments. We thank Thomas Comptdaer for excellent immunofluorescence technical assistance. We are grateful to the IMPRT (Institut de Médecine Prédictive et de Recherche Thérapeutique, Lille, France) for access to the confocal microscopy platform and to M. Tardivel and A. Bongiovanni for their assistance with confocal microscopy analyses. We thank Vincent Demarecourt and Romain Perbet for providing human brain tissues from the Lille Neurobank (CHRU-Lille, France). We express gratitude to the patients with Alzheimer disease and their families who allowed us to perform brain autopsies. We thank Dr. Miriam Sander for editorial assistance.

This work was, in part, supported by the National Institute on Aging, NIH (V.A.B., D.L.C., B.O., B.Y., and Y.W.). This work was supported by an NIA AD Concept grant from the National Institute on Aging (V.A.B., AG000578). This work was supported by a grant from Olav Thon Stiftelsen to L.J.R., V.A.B., J.L., and T.T. L.J.R. and C.D. were supported by Nordea-fonden. T.R., M.S., and T.T. were supported by the Norwegian Research Council (NORBRAIN project 197467). This work was also supported by Labex (Excellence Laboratory) – Development of Innovative Strategies for a Transdisciplinary Approach to Alzheimer’s disease [DISTALZ]. V.A.B. and M.-C.G. are also supported by INSTALZ, an EU Joint Program - Neurodegenerative Disease Research (JPND) project. The INSTALZ project is supported through the following funding organizations under the aegis of JPND - “<http://www.jpnd.eu>” www.jpnd.eu (Belgium, Research Foundation Flanders; Denmark, Innovation Fund Denmark; France, Agence Nationale de la Recherche; Sweden, Swedish Research Council; and United Kingdom, Medical Research Council). The project has received funding from the European Union’s Horizon 2020 Research and Innovation Program under grant agreement No 643417.

AUTHOR CONTRIBUTIONS

Conceptualization and designed of the study done by J.L., D.L.C., V.A.B., T.T., J.F.N., and L.J.R. J.F.N. conducted the bioinformatics analysis with input from D.L.C. A.J. and Z.A. processed and imaged the tissues for S.T. B.Y. performed the smelling tests. Y.W. carried out the LTP analysis. B.O. assisted with the western blotting. T.T., T.R., and M.S. performed the mass spectrometry, and T.T., T.R., M.S., J.F.N., and D.L.C. performed data analysis. M.-C.G. performed immunohistochemistry on human AD brains. D.L.C. and J.F.N. wrote the original draft, and all other authors reviewed and edited the manuscript. Supervision was provided by V.A.B., J.L., and T.T. Funding acquisition, V.A.B., J.L., T.T., L.J.R., and M.-C.G.

DECLARATION OF INTERESTS

J.L. and J.F.N. are scientific advisors at 10x Genomics Inc, which provides commercial barcoded arrays. All other authors declare no competing interests.

Received: June 4, 2020

Revised: August 24, 2020

Accepted: September 9, 2020

Published: October 23, 2020

REFERENCES

- Angeloni, C., Zamboni, L., and Hrelia, S. (2014). Role of methylglyoxal in Alzheimer’s disease. *Biomed. Res. Int.* *2014*, 238485.
- Bartholomeusz, G., Wu, Y., Ali Seyed, M., Xia, W., Kwong, K.Y., Hortobagyi, G., and Hung, M.C. (2006). Nuclear translocation of the pro-apoptotic Bcl-2 family member Bok induces apoptosis. *Mol. Carcinog* *45*, 73–83.
- Berglund, E., Maaskola, J., Schultz, N., Friedrich, S., Marklund, M., Bergenstrahle, J., Tarish, F., Tanoglidis, A., Vickovic, S., Larsson, L., et al. (2018). Spatial maps of prostate cancer transcriptomes reveal an unexplored landscape of heterogeneity. *Nat. Commun.* *9*, 2419.
- Blalock, E.M., Geddes, J.W., Chen, K.C., Porter, N.M., Markesbery, W.R., and Landfield, P.W. (2004). Incipient Alzheimer’s disease: microarray correlation analyses reveal major transcriptional and tumor suppressor responses. *Proc. Natl. Acad. Sci. U S A* *101*, 2173–2178.
- Burgess, D.J. (2019). Spatial transcriptomics coming of age. *Nat. Rev. Genet.* *20*, 317.
- Caruana, D.A., Alexander, G.M., and Dudek, S.M. (2012). New insights into the regulation of synaptic plasticity from an unexpected place: hippocampal area CA2. *Learn Mem.* *19*, 391–400.

- Chen, R., Yang, L., and McIntyre, T.M. (2007). Cytotoxic phospholipid oxidation products. Cell death from mitochondrial damage and the intrinsic caspase cascade. *J. Biol. Chem.* **282**, 24842–24850.
- Chen, W.T., Lu, A., Craessaerts, K., Pavie, B., Sala Frigerio, C., Corthout, N., Qian, X., Lalakova, J., Kuhnemund, M., Voytyuk, I., et al. (2020). Spatial transcriptomics and in situ sequencing to study Alzheimer's disease. *Cell* **4**, 976–991.e19.
- Cisse, M., Duplan, E., Lorivel, T., Dunys, J., Bauer, C., Meckler, X., Gerakis, Y., Lauritzen, I., and Checler, F. (2017). The transcription factor XBP1s restores hippocampal synaptic plasticity and memory by control of the Kalirin-7 pathway in Alzheimer model. *Mol. Psychiatry* **22**, 1562–1575.
- D'Orsi, B., Engel, T., Pfeiffer, S., Nandi, S., Kaufmann, T., Henshall, D.C., and Prehn, J.H. (2016). Bok is not pro-apoptotic but suppresses poly ADP-ribose polymerase-dependent cell death pathways and protects against excitotoxic and seizure-induced neuronal injury. *J. Neurosci.* **36**, 4564–4578.
- D'Orsi, B., Matelyka, J., and Prehn, J.H.M. (2017). Control of mitochondrial physiology and cell death by the Bcl-2 family proteins Bax and Bok. *Neurochem. Int.* **109**, 162–170.
- Del-Aguila, J.L., Li, Z., Dube, U., Mihindukulasuriya, K.A., Budde, J.P., Fernandez, M.V., Ibanez, L., Bradley, J., Wang, F., Bergmann, K., et al. (2019). A single-nuclei RNA sequencing study of Mendelian and sporadic AD in the human brain. *Alzheimers Res. Ther.* **11**, 71.
- Demarest, T.G., Varma, V.R., Estrada, D., Babbar, M., Basu, S., Mahajan, U.V., Moaddel, R., Croteau, D.L., Thambisetty, M., Mattson, M.P., et al. (2020). Biological sex and DNA repair deficiency drive Alzheimer's disease via systemic metabolic remodeling and brain mitochondrial dysfunction. *Acta Neuropathol.* **140**, 25–47.
- Desler, C., Lillenes, M.S., Tonjum, T., and Rasmussen, L.J. (2017). The role of mitochondrial dysfunction in the progression of Alzheimer's disease. *Curr. Med. Chem.* **40**, 5578–5587.
- Dixon, C., Sah, P., Lynch, J.W., and Keramidas, A. (2014). GABAA receptor alpha and gamma subunits shape synaptic currents via different mechanisms. *J. Biol. Chem.* **289**, 5399–5411.
- Einsele-Scholz, S., Malmshaimer, S., Bertram, K., Stehle, D., Johanning, J., Manz, M., Daniel, P.T., Gillissen, B.F., Schulze-Osthoff, K., and Essmann, F. (2016). Bok is a genuine multi-BH-domain protein that triggers apoptosis in the absence of Bax and Bak. *J. Cell Sci.* **129**, 2213–2223.
- Fang, E.F., Hou, Y., Palikaras, K., Adriaanse, B.A., Kerr, J.S., Yang, B., Lautrup, S., Hasan-Olive, M.M., Caponio, D., Dan, X., et al. (2019). Mitophagy inhibits amyloid-beta and tau pathology and reverses cognitive deficits in models of Alzheimer's disease. *Nat. Neurosci.* **22**, 401–412.
- Frandsen, J.R., and Narayanasamy, P. (2018). Neuroprotection through flavonoid: enhancement of the glyoxalase pathway. *Redox Biol.* **14**, 465–473.
- Glykys, J., and Mody, I. (2006). Hippocampal network hyperactivity after selective reduction of tonic inhibition in GABA A receptor alpha5 subunit-deficient mice. *J. Neurophysiol.* **95**, 2796–2807.
- Grubman, A., Chew, G., Ouyang, J.F., Sun, G., Choo, X.Y., McLean, C., Simmons, R.K., Buckberry, S., Vargas-Landin, D.B., Poppe, D., et al. (2019). A single-cell atlas of entorhinal cortex from individuals with Alzheimer's disease reveals cell-type-specific gene expression regulation. *Nat. Neurosci.* **22**, 2087–2097.
- Hirata-Fukae, C., Li, H.F., Hoe, H.S., Gray, A.J., Minami, S.S., Hamada, K., Niikura, T., Hua, F., Tsukagoshi-Nagai, H., Horikoshi-Sakuraba, Y., et al. (2008). Females exhibit more extensive amyloid, but not tau, pathology in an Alzheimer transgenic model. *Brain Res.* **1216**, 92–103.
- Hiroi, N., Brown, J.R., Haile, C.N., Ye, H., Greenberg, M.E., and Nestler, E.J. (1997). FosB mutant mice: loss of chronic cocaine induction of Fos-related proteins and heightened sensitivity to cocaine's psychomotor and rewarding effects. *Proc. Natl. Acad. Sci. U S A* **94**, 10397–10402.
- Hou, Y., Lautrup, S., Cordonnier, S., Wang, Y., Croteau, D.L., Zavala, E., Zhang, Y., Moritoh, K., O'Connell, J.F., Baptiste, B.A., et al. (2018). NAD(+) supplementation normalizes key Alzheimer's features and DNA damage responses in a new AD mouse model with introduced DNA repair deficiency. *Proc. Natl. Acad. Sci. U S A* **115**, E1876–E1885.
- Jardin, I., Lopez, J.J., Berna-Erro, A., Salido, G.M., and Rosado, J.A. (2013). Homer proteins in Ca(2)(+) entry. *IUBMB Life* **65**, 497–504.
- Johnson, E.C.B., Dammer, E.B., Duong, D.M., Yin, L., Thambisetty, M., Troncoso, J.C., Lah, J.J., Levey, A.I., and Seyfried, N.T. (2018). Deep proteomic network analysis of Alzheimer's disease brain reveals alterations in RNA binding proteins and RNA splicing associated with disease. *Mol. Neurodegener.* **13**, 52.
- Johnstone, V.P., and Raymond, C.R. (2013). Postsynaptic protein synthesis is required for presynaptic enhancement in persistent forms of long-term potentiation. *Front. Synaptic Neurosci.* **5**, 1.
- Kam, T.I., Mao, X., Park, H., Chou, S.C., Karuppagounder, S.S., Umanah, G.E., Yun, S.P., Brahmachari, S., Panicker, N., Chen, R., et al. (2018). Poly(ADP-ribose) drives pathologic alpha-synuclein neurodegeneration in Parkinson's disease. *Science* **362**, eaat8407.
- Keren-Shaul, H., Spinrad, A., Weiner, A., Matcovitch-Natan, O., Dvir-Szternfeld, R., Ulland, T.K., David, E., Baruch, K., Lara-Astaiso, D., Toth, B., et al. (2017). A unique microglia type Associated with restricting development of Alzheimer's disease. *Cell* **169**, 1276–1290.e17.
- Kuhla, B., Boeck, K., Schmidt, A., Ogunlade, V., Arendt, T., Munch, G., and Luth, H.J. (2007). Age- and stage-dependent glyoxalase I expression and its activity in normal and Alzheimer's disease brains. *Neurobiol. Aging* **28**, 29–41.
- Lang, F., Stouraras, C., Zacharopoulou, N., Voelkl, J., and Alesutan, I. (2018). Serum- and glucocorticoid-inducible kinase 1 and the response to cell stress. *Cell Stress* **3**, 1–8.
- Liotta, A., Rosner, J., Huchzermeyer, C., Wojtowicz, A., Kann, O., Schmitz, D., Heinemann, U., and Kovacs, R. (2012). Energy demand of synaptic transmission at the hippocampal Schaffer-collateral synapse. *J. Cereb. Blood Flow Metab.* **32**, 2076–2083.
- Liu, D., Lu, H., Stein, E., Zhou, Z., Yang, Y., and Mattson, M.P. (2018). Brain regional synchronous activity predicts tauopathy in 3xTgAD mice. *Neurobiol. Aging* **70**, 160–169.
- Llambi, F., Wang, Y.M., Victor, B., Yang, M., Schneider, D.M., Gingras, S., Parsons, M.J., Zheng, J.H., Brown, S.A., Pelletier, S., et al. (2016). BOK is a non-canonical BCL-2 family effector of apoptosis regulated by ER-associated degradation. *Cell* **165**, 421–433.
- Llorian, M., Beullens, M., Andres, I., Ortiz, J.M., and Bollen, M. (2004). SIPP1, a novel pre-mRNA splicing factor and interactor of protein phosphatase-1. *Biochem. J.* **378**, 229–238.
- Maaskola, J., Bergenstrahle, L., Jurek, A., Navarro, J.F., Lagergren, J., and Lundeberg, J. (2018). Charting tissue expression anatomy by spatial transcriptome decomposition. *bioRxiv*. <https://doi.org/10.1101/362624>.
- Maniatis, S., Aijo, T., Vickovic, S., Braine, C., Kang, K., Mollbrink, A., Fagegaltier, D., Andrusivova, Z., Saarenpaa, S., Saiz-Castro, G., et al. (2019). Spatiotemporal dynamics of molecular pathology in amyotrophic lateral sclerosis. *Science* **364**, 89–93.
- Martinez-Lopez, M.J., Alcantara, S., Mascaró, C., Perez-Branguli, F., Ruiz-Lozano, P., Maes, T., Soriano, E., and Buesa, C. (2005). Mouse neuron navigator 1, a novel microtubule-associated protein involved in neuronal migration. *Mol. Cell Neurosci.* **28**, 599–612.
- Mattson, M.P., Guthrie, P.B., and Kater, S.B. (1989). Intrinsic factors in the selective vulnerability of hippocampal pyramidal neurons. *Prog. Clin. Biol. Res.* **317**, 333–351.
- McClard, C.K., Kochukov, M.Y., Herman, I., Liu, Z., Eblimit, A., Moayed, Y., Ortiz-Guzman, J., Colchado, D., Pekarek, B., Panneerselvam, S., et al. (2018). POU6f1 mediates neuropeptide-dependent plasticity in the adult brain. *J. Neurosci.* **38**, 1443–1461.
- Misiak, M., Vergara Greeno, R., Baptiste, B.A., Sykora, P., Liu, D., Cordonnier, S., Fang, E.F., Croteau, D.L., Mattson, M.P., and Bohr, V.A. (2017a). DNA polymerase beta decrement triggers death of olfactory bulb cells and impairs olfaction in a mouse model of Alzheimer's disease. *Aging Cell* **16**, 162–172.
- Misiak, M.M., Hipolito, M.S., Ransom, H.W., Obisesan, T.O., Manaye, K.F., and Nwulia, E.A. (2017b). Apo E4 alleles and impaired olfaction as predictors of Alzheimer's disease. *Clin. Exp. Psychol.* **3**, 169.
- Mosconi, L., Pupi, A., and De Leon, M.J. (2008). Brain glucose hypometabolism and oxidative stress in preclinical Alzheimer's disease. *Ann. N. Y. Acad. Sci.* **1147**, 180–195.
- Murphy, C. (2019). Olfactory and other sensory impairments in Alzheimer disease. *Nat. Rev. Neurol.* **15**, 11–24.

Nishitsuji, K., Hosono, T., Uchimura, K., and Michikawa, M. (2011). Lipoprotein lipase is a novel amyloid beta (A β)-binding protein that promotes glycosaminoglycan-dependent cellular uptake of A β in astrocytes. *J. Biol. Chem.* *286*, 6393–6401.

Oliver, P.L., Finelli, M.J., Edwards, B., Bitoun, E., Butts, D.L., Becker, E.B., Cheeseman, M.T., Davies, B., and Davies, K.E. (2011). Oxr1 is essential for protection against oxidative stress-induced neurodegeneration. *Plos Genet.* *7*, e1002338.

Paillasse, M.R., and de Medina, P. (2015). The NR4A nuclear receptors as potential targets for anti-aging interventions. *Med. Hypotheses* *84*, 135–140.

Pandey, K.N. (2018). Molecular and genetic aspects of guanylyl cyclase natriuretic peptide receptor-A in regulation of blood pressure and renal function. *Physiol. Genomics* *50*, 913–928.

Patel, H., Dobson, R.J.B., and Newhouse, S.J. (2019). A meta-analysis of Alzheimer's disease brain transcriptomic data. *J. Alzheimers Dis.* *68*, 1635–1656.

Rahayel, S., Frasnelli, J., and Joubert, S. (2012). The effect of Alzheimer's disease and Parkinson's disease on olfaction: a meta-analysis. *Behav. Brain Res.* *231*, 60–74.

Regard, J.B., Scheek, S., Borbiev, T., Lanahan, A.A., Schneider, A., Demetriades, A.M., Hiemisch, H., Barnes, C.A., Verin, A.D., and Worley, P.F. (2004). Verge: a novel vascular early response gene. *J. Neurosci.* *24*, 4092–4103.

Reynolds, M.S., Hancock, C.R., Ray, J.D., Kener, K.B., Draney, C., Garland, K., Hardman, J., Bikman, B.T., and Tessem, J.S. (2016). beta-Cell

deletion of Nr4a1 and Nr4a3 nuclear receptors impedes mitochondrial respiration and insulin secretion. *Am. J. Physiol. Endocrinol. Metab.* *311*, E186–E201.

Rissman, R.A., De Blas, A.L., and Armstrong, D.M. (2007). GABA(A) receptors in aging and Alzheimer's disease. *J. Neurochem.* *103*, 1285–1292.

Rodrigues, S.G., Stickels, R.R., Goeva, A., Martin, C.A., Murray, E., Vanderburg, C.R., Welch, J., Chen, L.M., Chen, F., and Macosko, E.Z. (2019). Slide-seq: a scalable technology for measuring genome-wide expression at high spatial resolution. *Science* *363*, 1463–1467.

Schulman, J.J., Szczesniak, L.M., Bunker, E.N., Nelson, H.A., Roe, M.W., Wagner, L.E., 2nd, Yule, D.I., and Wojcikiewicz, R.J.H. (2019). Bok regulates mitochondrial fusion and morphology. *Cell Death Differ* *1121*, 2682–2694.

Shi, J., Kahle, A., Hershey, J.W., Honchak, B.M., Warneke, J.A., Leong, S.P., and Nelson, M.A. (2006). Decreased expression of eukaryotic initiation factor 3f deregulates translation and apoptosis in tumor cells. *Oncogene* *25*, 4923–4936.

Srivastava, R., Cao, Z., Nedeva, C., Naim, S., Bachmann, D., Rabachini, T., Gangoda, L., Shahi, S., Glab, J., Menassa, J., et al. (2019). BCL-2 family protein BOK is a positive regulator of uridine metabolism in mammals. *Proc. Natl. Acad. Sci. U S A* *116*, 15469–15474.

Stahl, P.L., Salmen, F., Vickovic, S., Lundmark, A., Navarro, J.F., Magnusson, J., Giacomello, S., Asp, M., Westholm, J.O., Huss, M., et al. (2016). Visualization and analysis of gene expression in tissue sections by spatial transcriptomics. *Science* *353*, 78–82.

Swerdlow, R.H. (2018). Mitochondria and mitochondrial cascades in Alzheimer's disease. *J. Alzheimers Dis.* *1403–1416*.

Sykora, P., Misiak, M., Wang, Y., Ghosh, S., Leandro, G.S., Liu, D., Tian, J., Baptiste, B.A., Cong, W.N., Brennerman, B.M., et al. (2015). DNA polymerase beta deficiency leads to neurodegeneration and exacerbates Alzheimer disease phenotypes. *Nucleic Acids Res.* *43*, 943–959.

Ullrich, S., Munch, A., Neumann, S., Kremmer, E., Tatzelt, J., and Lichtenthaler, S.F. (2010). The novel membrane protein TMEM59 modulates complex glycosylation, cell surface expression, and secretion of the amyloid precursor protein. *J. Biol. Chem.* *285*, 20664–20674.

Vickovic, S., Eraslan, G., Salmen, F., Klughammer, J., Stenbeck, L., Schapiro, D., Aijo, T., Bonneau, R., Bergenstrahle, L., Navarro, J.F., et al. (2019). High-definition spatial transcriptomics for in situ tissue profiling. *Nat. Methods* *16*, 987–990.

Weissman, L., Jo, D.G., Sorensen, M.M., de Souza-Pinto, N.C., Marquesbery, W.R., Mattson, M.P., and Bohr, V.A. (2007). Defective DNA base excision repair in brain from individuals with Alzheimer's disease and amnesic mild cognitive impairment. *Nucleic Acids Res.* *35*, 5545–5555.

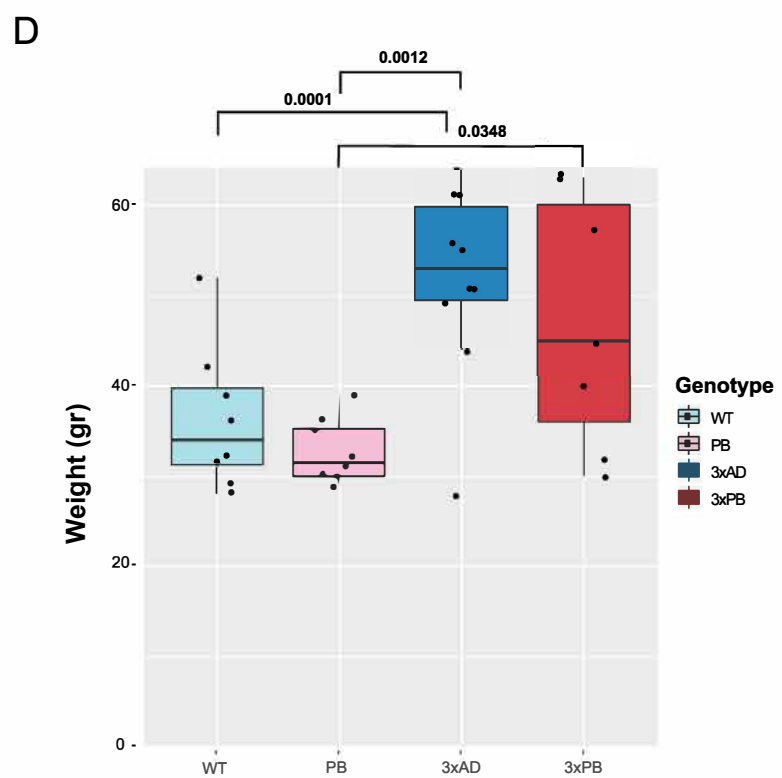
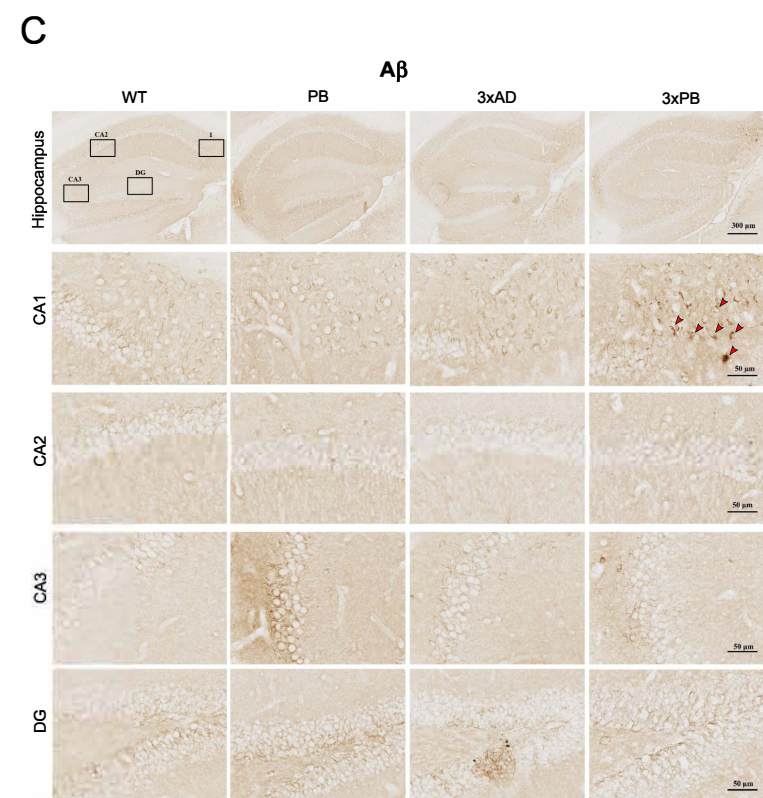
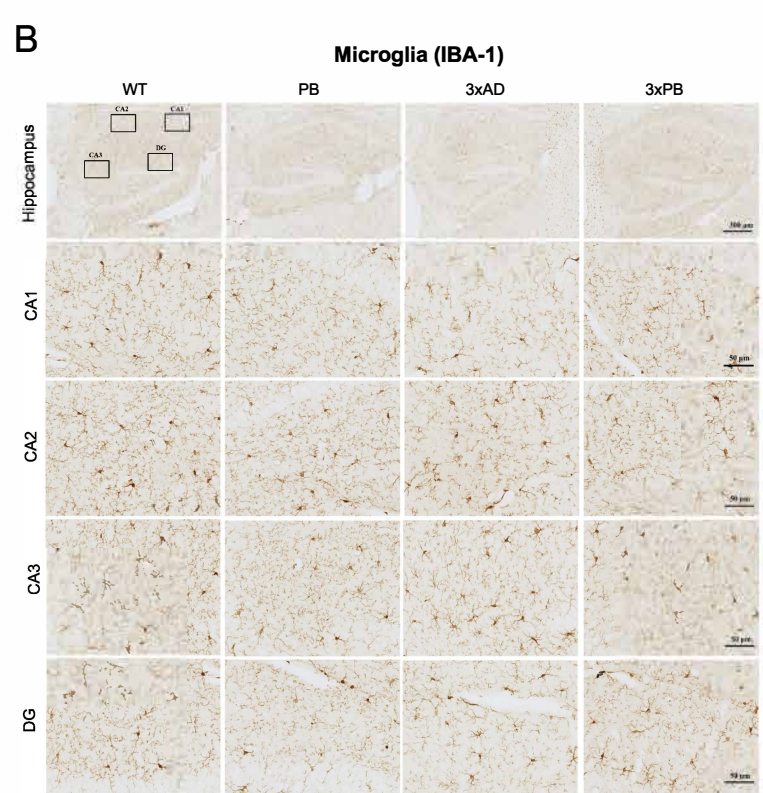
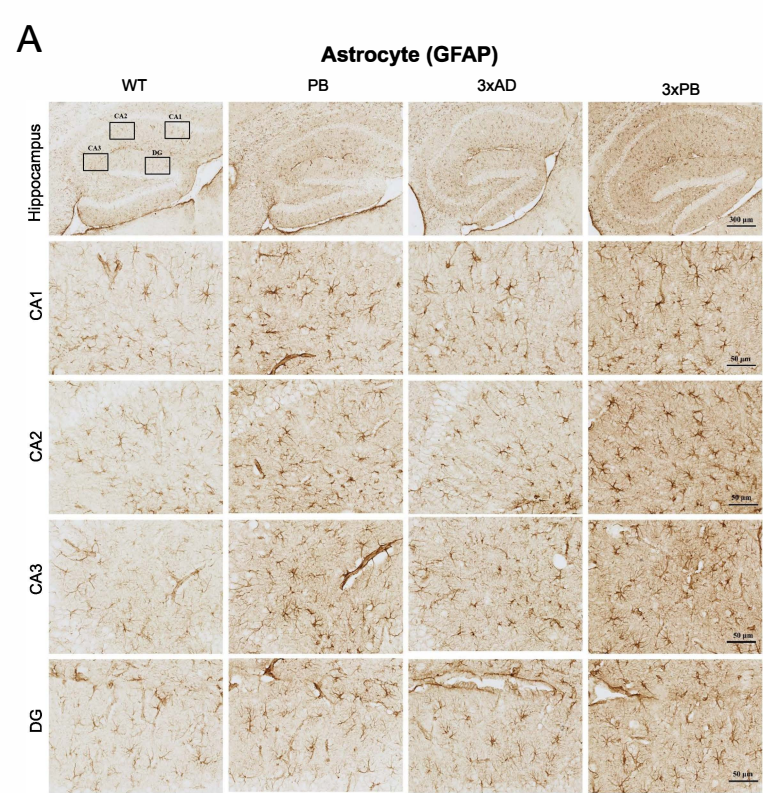
Zheng, J.H., Grace, C.R., Guibao, C.D., McNamara, D.E., Llambi, F., Wang, Y.M., Chen, T., and Moldoveanu, T. (2018). Intrinsic instability of BOK enables membrane permeabilization in apoptosis. *Cell Rep.* *23*, 2083–2094.e6.

Zheng, Q., Zheng, X., Zhang, L., Luo, H., Qian, L., Fu, X., Liu, Y., Gao, Y., Niu, M., Meng, J., et al. (2017). The neuron-specific protein TMEM59L mediates oxidative stress-induced cell death. *Mol. Neurobiol.* *54*, 4189–4200.

Supplemental Information

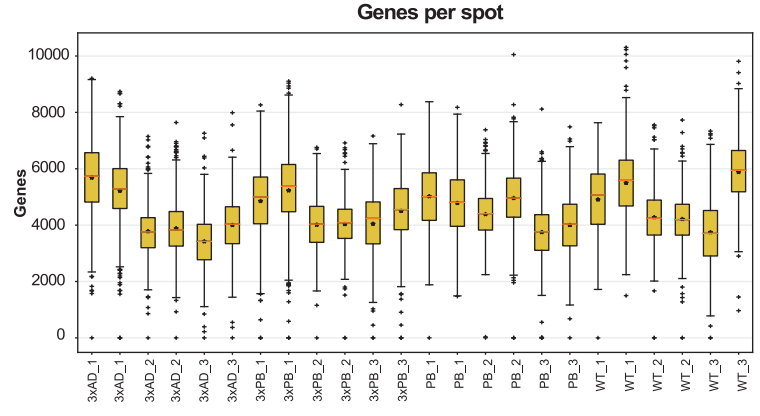
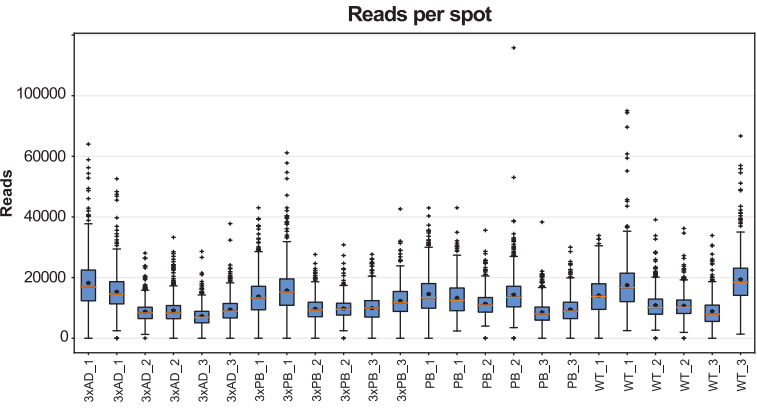
Spatial Transcriptomics Reveals Genes Associated with Dysregulated Mitochondrial Functions and Stress Signaling in Alzheimer Disease

José Fernández Navarro, Deborah L. Croteau, Aleksandra Jurek, Zaneta Andrusivova, Beimeng Yang, Yue Wang, Benjamin Ogedegbe, Tahira Riaz, Mari Støen, Claus Desler, Lene Juel Rasmussen, Tone Tønjum, Marie-Christine Galas, Joakim Lundeberg, and Vilhelm A. Bohr



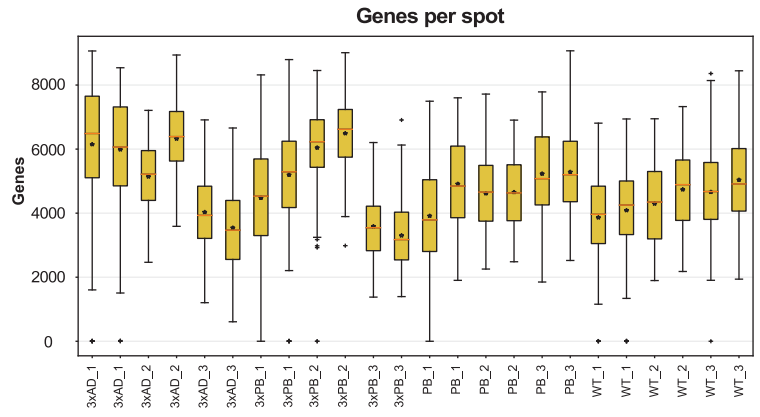
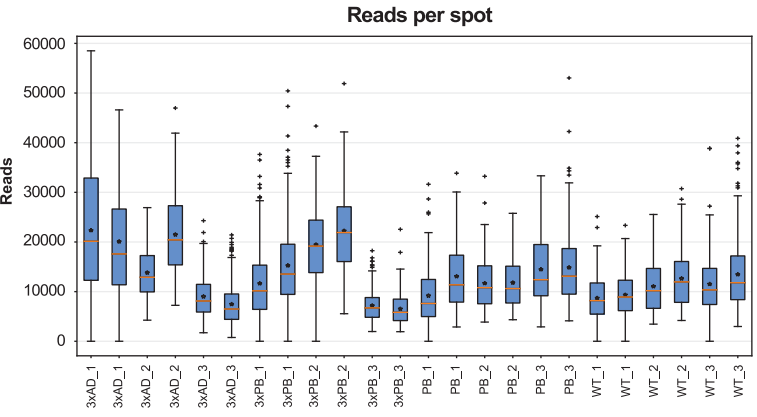
A

Hippocampus

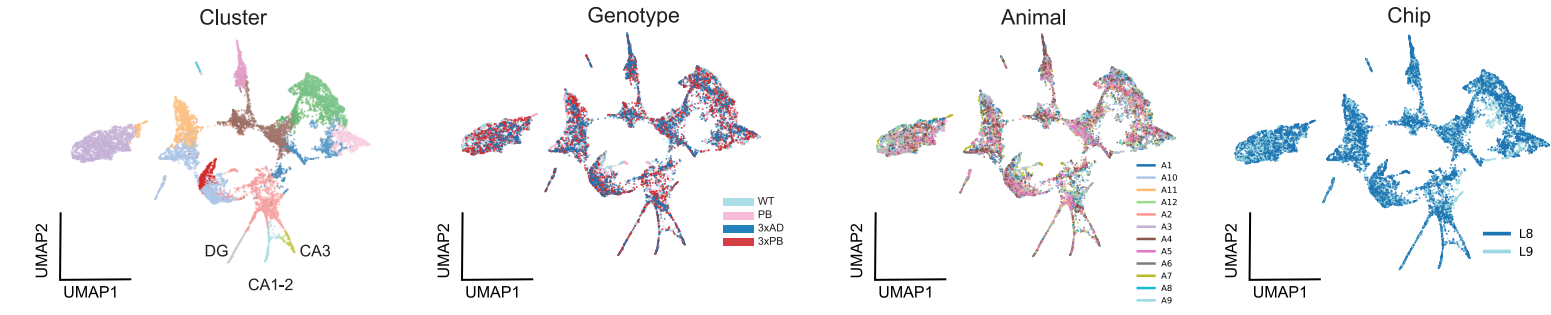


B

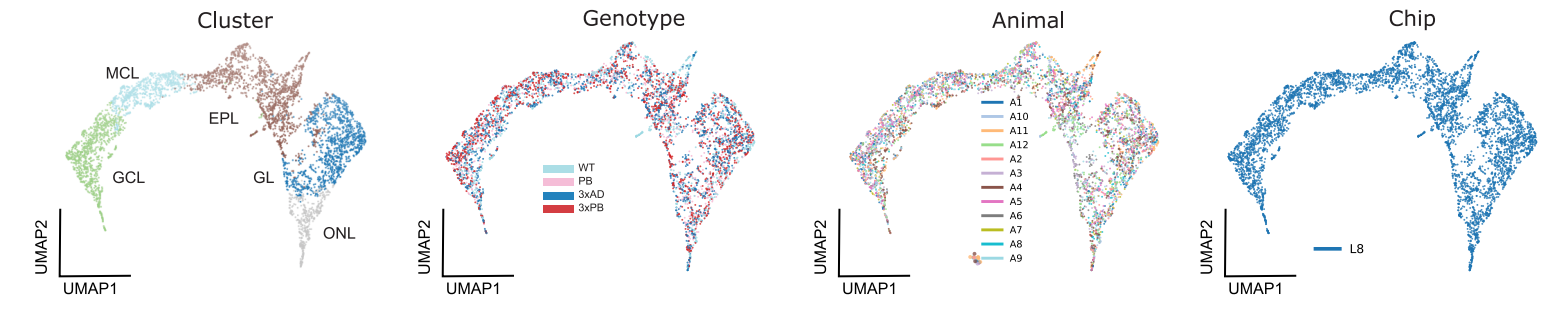
Olfactory bulb

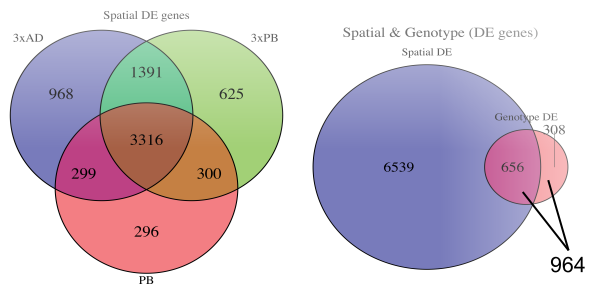
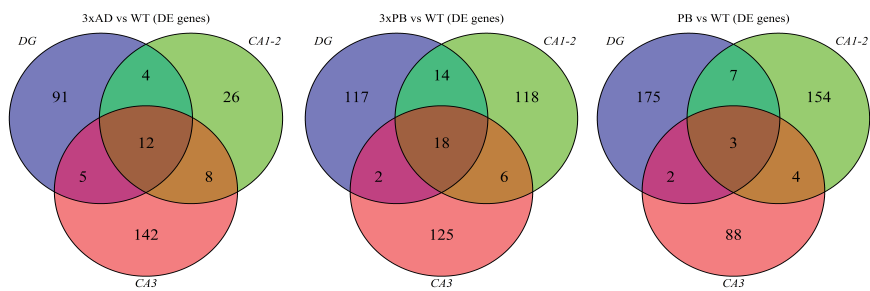
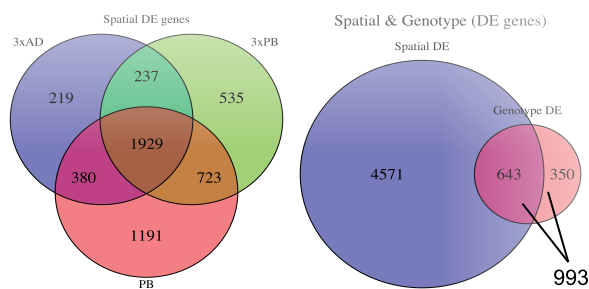
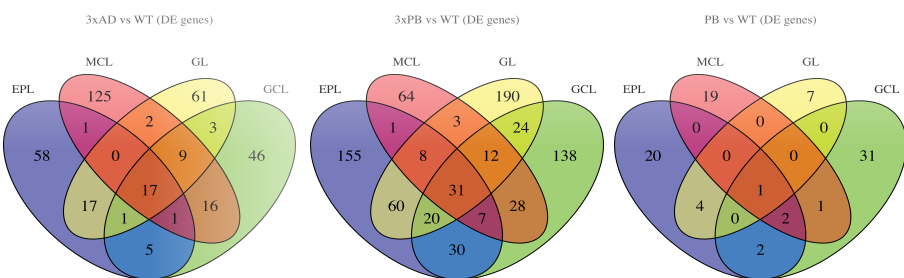
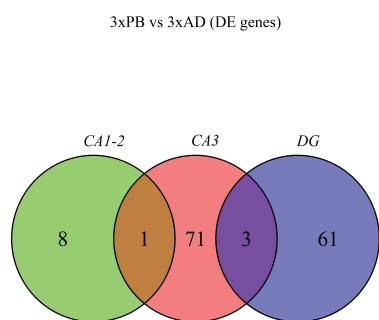
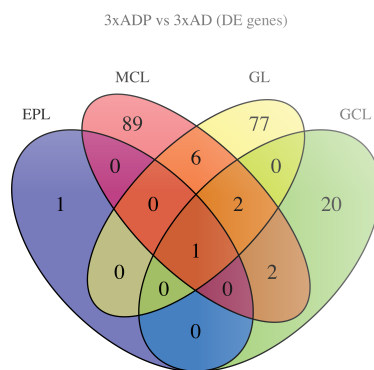
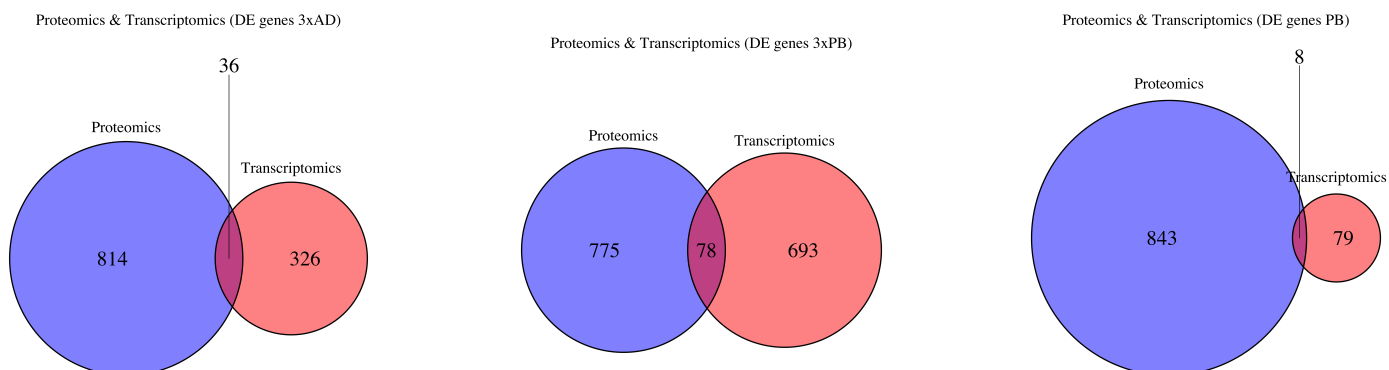


C



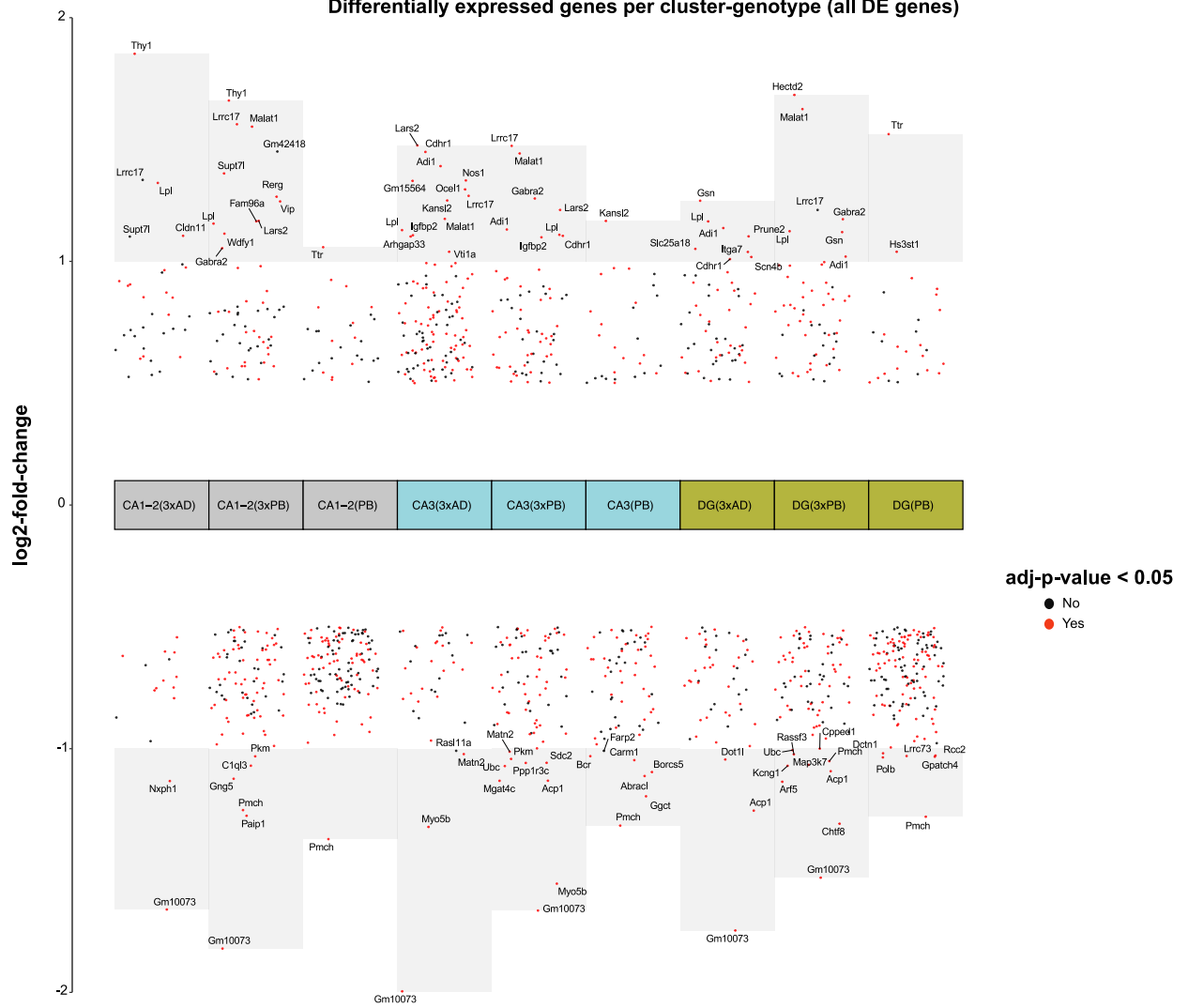
D



A**B****C****D****E****F****G**

A

Differentially expressed genes per cluster-genotype (all DE genes)

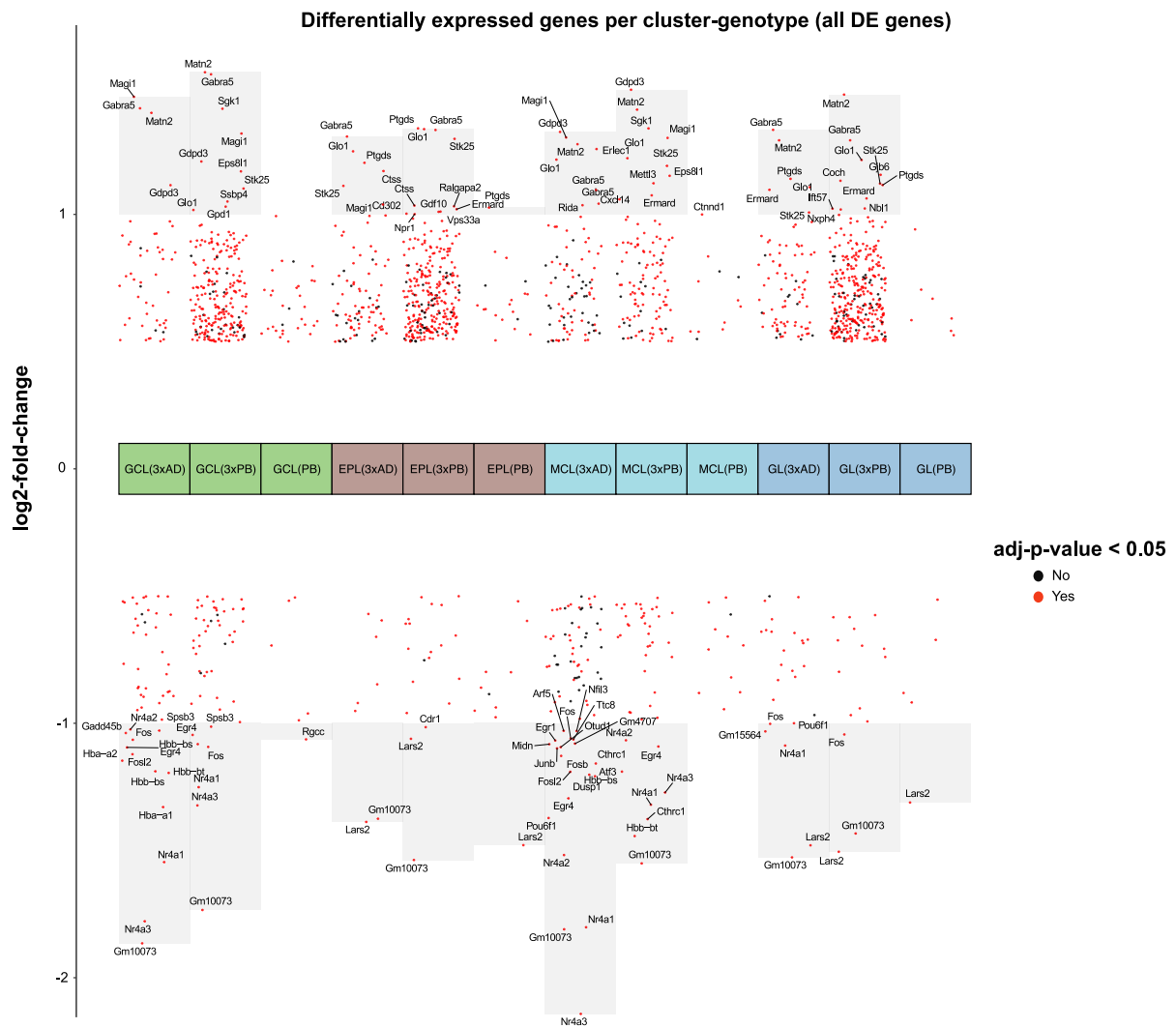


B

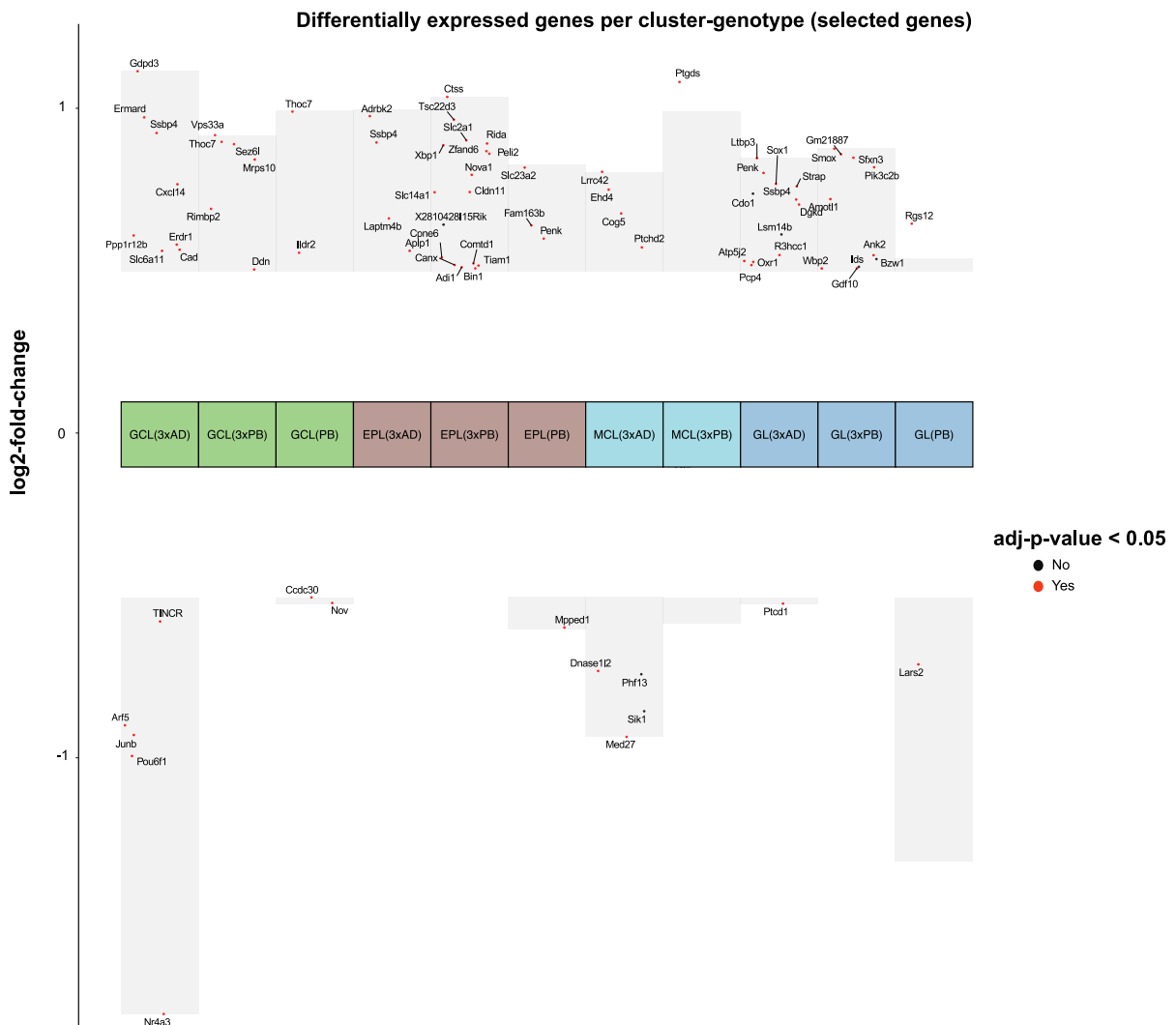
Differentially expressed genes per cluster-genotype (selected genes)



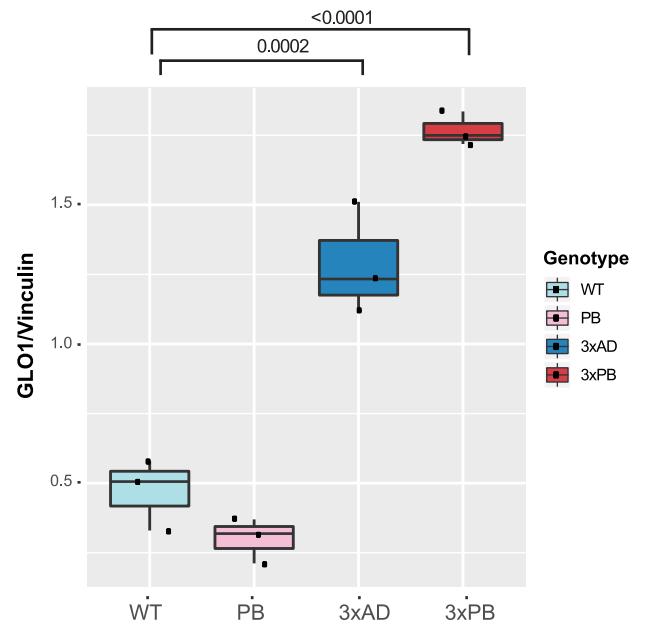
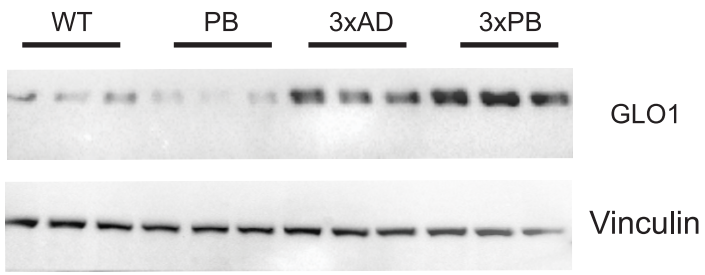
A



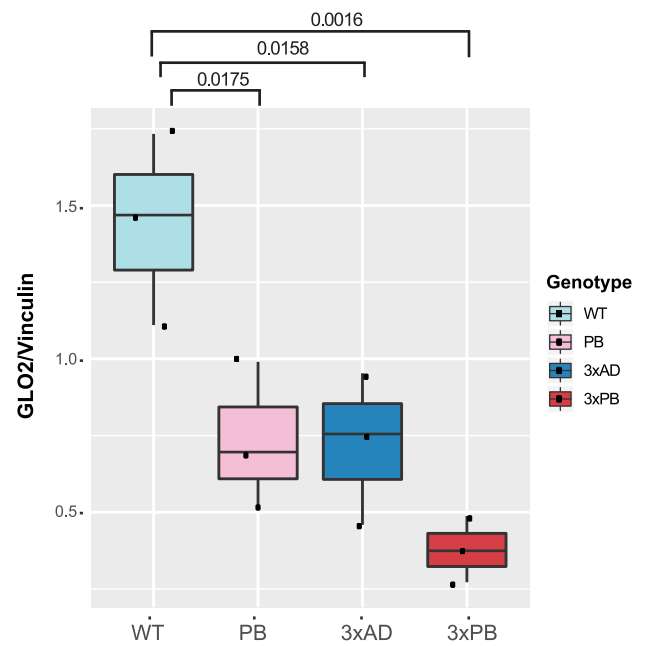
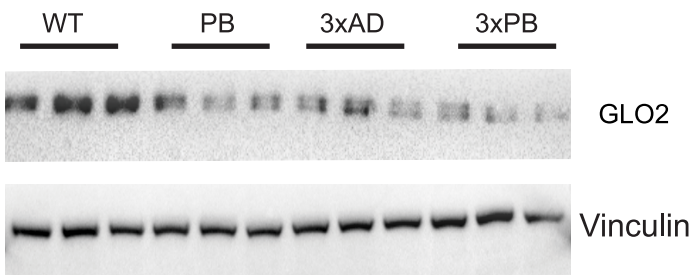
B

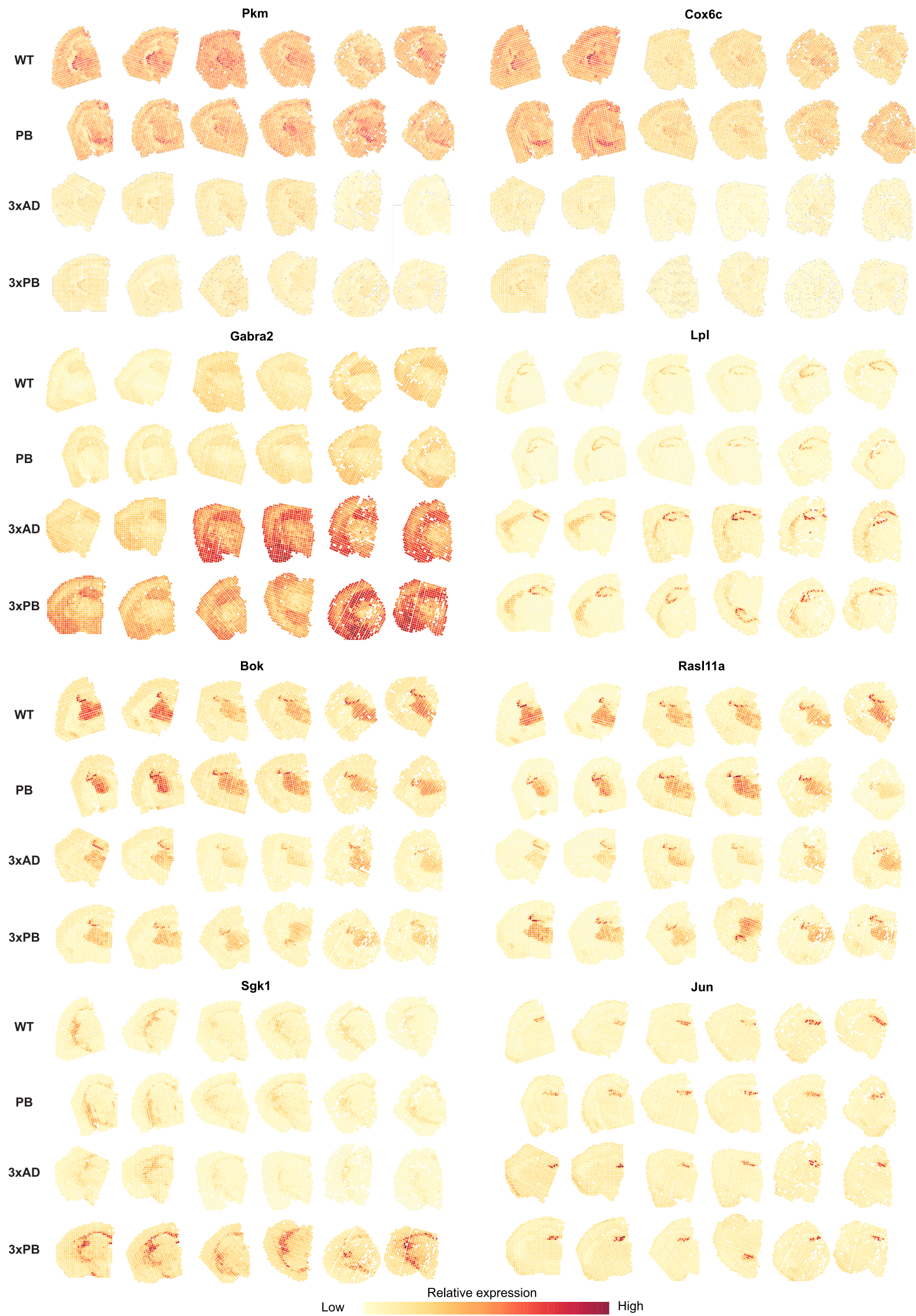


A



B



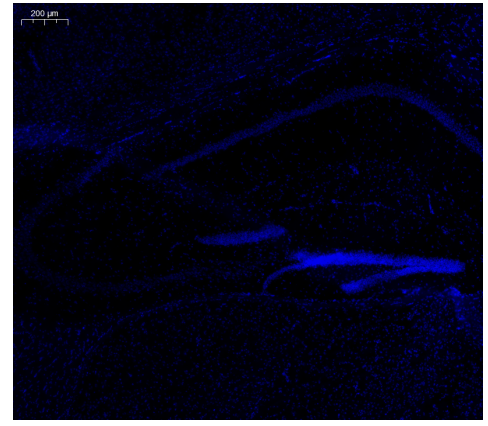
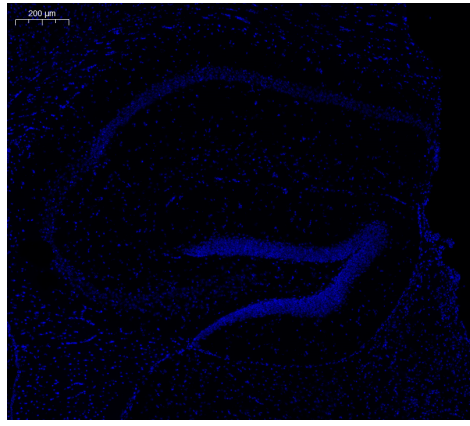
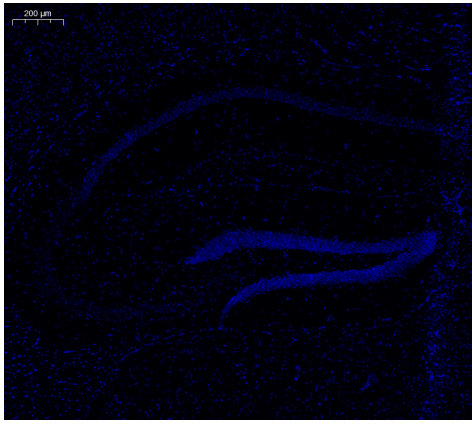


WT

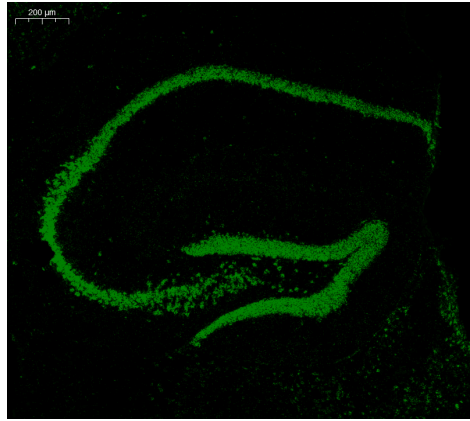
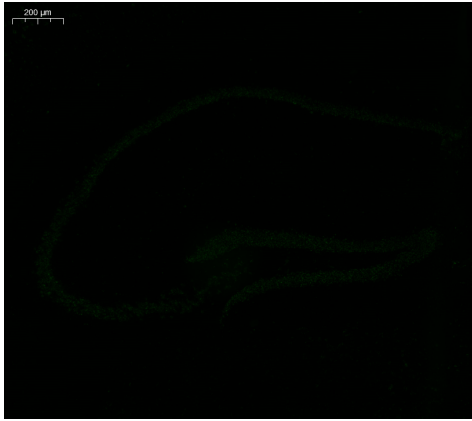
3xAD

Neg. control

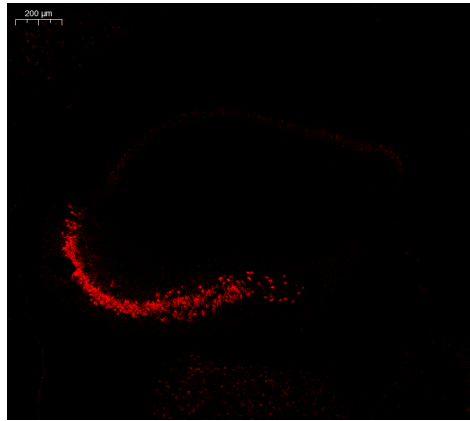
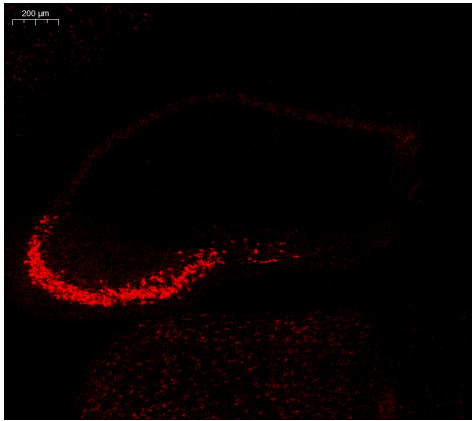
DAPI



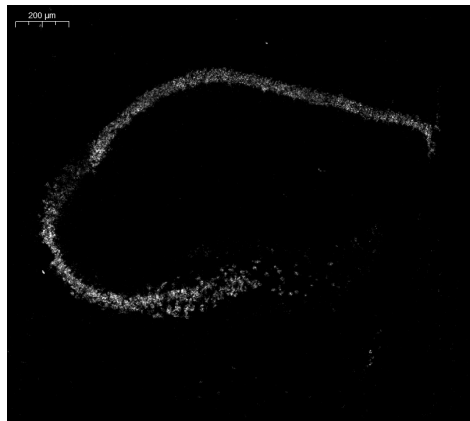
Gabra2



Bok



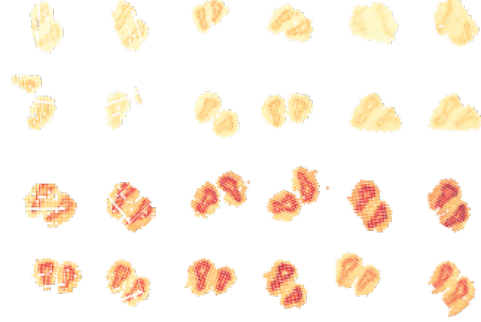
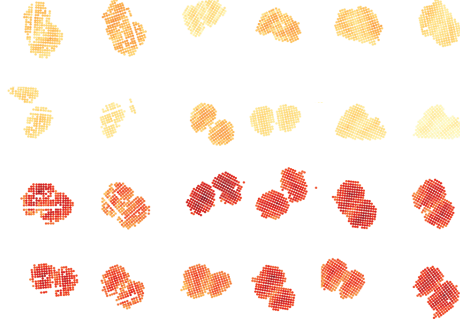
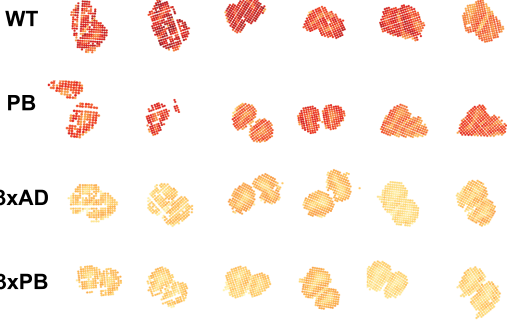
Lpl



Cox6c

Fam32a

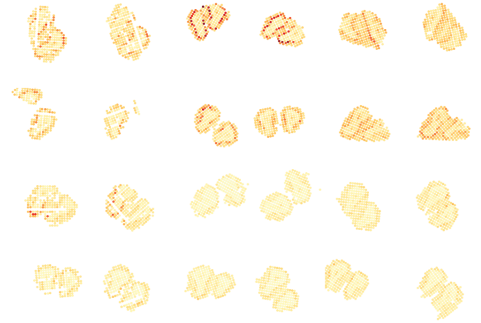
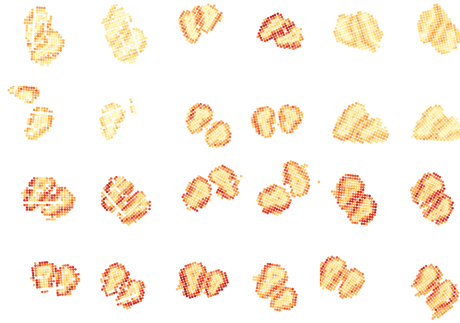
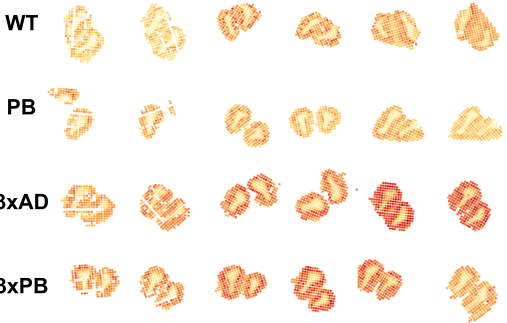
Gabra5



Oxr1

Nav1

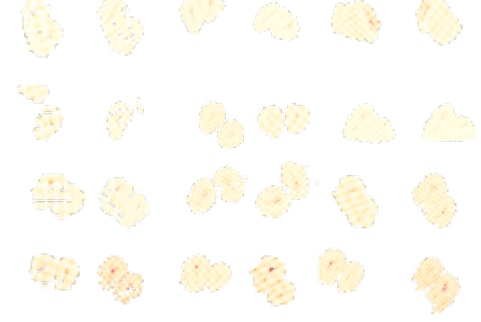
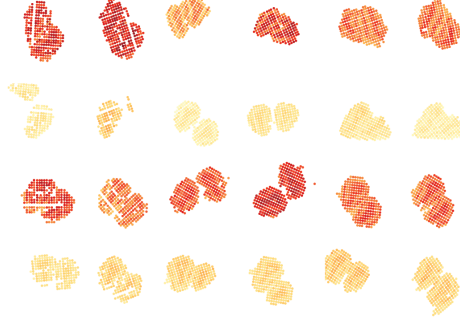
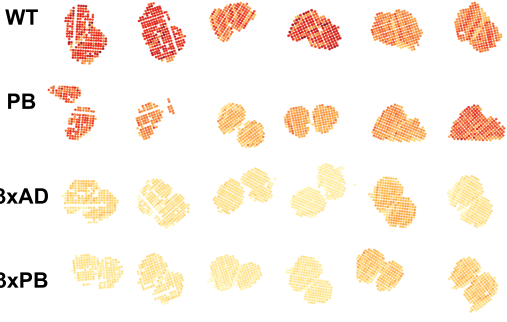
Pla2g7



Pou6f1

PolB

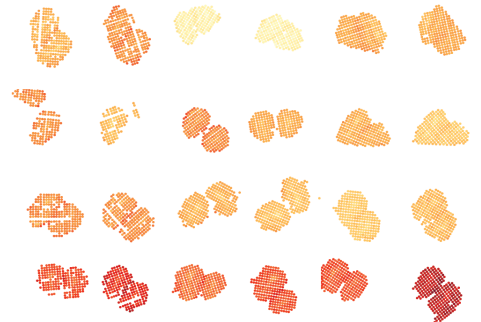
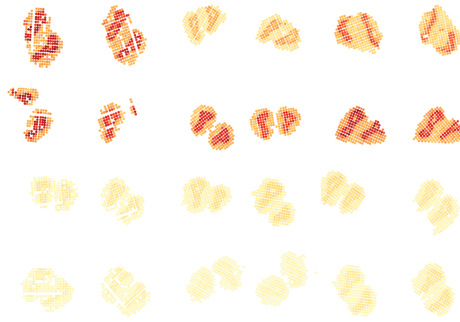
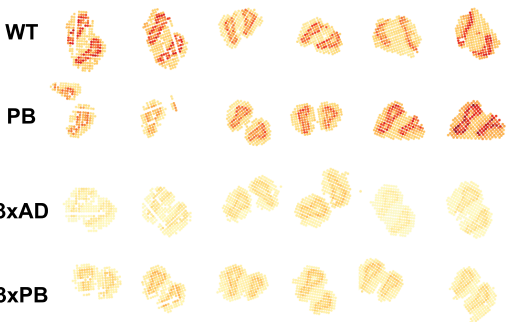
Sgk1




Fosb

Nr4a3

Xbp1



Low  High

Relative expression

Supplemental Figure Legends

Figure S1. Immunohistochemistry for astrocytes, microglia and A β are consistent with early AD pathology. See also Figure 1.

For immunohistochemistry, two mice per genotype were used for each analysis.

- A) Immunohistochemistry for GFAP, a marker for astrocytes, in the various brain areas by mouse genotype.
- B) Immunohistochemistry for Iba-1, a marker for microglia, in the various brain areas by mouse genotype.
- C) Immunohistochemistry for A β , in the various brain areas by mouse genotype. Arrows denote increased A β deposition in the subiculum.
- D) Mouse weights. One-way Anova with Dunnett post-hoc test was used to determine statistical significance. Error bars represent SEM.

Figure S2. Statistical summary of the datasets and QC. See also Figure 2.

- A) The number of reads and genes per spot obtained from the hippocampi are shown per mouse with two slices per mouse.
- B) The number of reads and genes per spot obtained from the OFBs are shown per mouse with two slices per mouse.
- C) UMAP manifolds of spots based on the factor activities and colored by cluster, genotype, animal, and chip (hippocampus).
- D) UMAP manifolds of spots based on factor activities and colored by cluster, genotype, animal, and chip (OFB).

Figure S3. Summary of the results of the differential expression analysis. See also Figure 3.

- A) Venn diagrams obtained from the highly confident spatially-differentially expressed genes in the hippocampus dataset. 964 genes were differentially expressed by genotype and 656 were DE spatially and by genotype.
- B) Venn diagrams obtained from the highly confident spatially-differentially expressed genes in the OFB dataset. 993 genes were differentially expressed by genotype and 643 were DE spatial and by genotype.
- C) Venn diagrams obtained from the highly confident differentially expressed genes in the hippocampus dataset for different genotypes and regions.
- D) Venn diagrams obtained from the highly confident differentially expressed genes in the OFB dataset for different genotypes and regions.
- E) Venn diagrams obtained from the highly confident differentially expressed genes in the hippocampus dataset for the direct comparison between 3xAD and 3xPB.
- F) Venn diagrams obtained from the highly confident differentially expressed genes in the OFB dataset for the direct comparison between 3xAD and 3xPB.
- G) Venn diagrams obtained from the shared proteomics and transcriptomics, all as compared to WT.

Figure S4. Volcano plots of DE genes derived from the hippocampus. See also Figure 4.

Due to space all the genes that have a adj. p-value ≤ 0.05 and fold-change ≥ 1.0 are labeled.

- A) Volcano plot of all highly confident DE genes from the hippocampus dataset, all as compared to WT.
- B) Volcano plot of just the select genes as shown in Figure 4.

Figure S5. Volcano plots of DE genes derived from the olfactory bulbs. See also Figure 5.

Due to space all the genes that have a adj. p-value ≤ 0.05 and fold-change ≥ 1.0 are labeled.

- A) Volcano plot of all highly confident DE genes from the OFB dataset, all as compared to WT.
- B) Volcano plot of just the select genes as shown in Figure 5

Figure S6. Validation of Glo1 and Glo2 protein expression. See also Figure 4.

- A) Western blots (Glo1 and Vinculin (loading control)) and quantification, labels in sets of three from left to right (WT, PB, 3xAD and 3xPB).
- B) Western blots (Glo2 and Vinculin (loading control)) and quantification, labels in sets of three from left to right (WT, PB, 3xAD and 3xPB).

Three mice were used per genotype. One-way Anova with Dunnett post-hoc test was used to determine statistical significance. Error bars represent SEM.

Figure S7. Top 25 hippocampal GO biological terms sorted by enrichment score. See also Figure 4.

- A) Enrichment scores using the top 25 terms derived from GO biological enrichment analysis on all highly confident DE genes in the hippocampus.
- B) Gene clustergram across the various GO terms from A.

Figure S8. Full graphic representation of select hippocampal gene plots from all mice. See also Figure 4. Graphic representation of a few hippocampal dataset gene's normalized expression data across all mice. Three mice were used per genotype, two slices per mouse, all are displayed. Images for *Pkm*, *Cox6c*, *Gabra2*, *Lpl*, *Bok*, *Ras111a*, *Sgk1* and *Jun* are shown. Due to space constraints all genes could not be shown.

Figure S9. RNAscope. See also Figure 4. RNAscope was conducted to visualize expression of *Gabra2*, *Bok*, and *Lpl*. WT and 3xAD brains were embedded into one block together, sliced, and probed for *Gabra2* (green), *Bok* (red) and *Lpl* (white) in a 3-plex reaction. A representative image is shown from two biological replicates. Scale bar is 200 μ m.

Figure S10. Top 25 olfactory bulb GO biological terms sorted by anatomic regions and genotype. See also Figure 5.

- A) Enrichment scores using the top 25 terms derived from GO biological enrichment analysis on all highly confident DE genes in the olfactory bulbs.
- B) Gene clustergram across the various GO terms from A.

Figure S11. Graphic representation of OFB gene plots from all mice. See also Figure 5. Graphic representation of a few OFB gene's normalized expression data across all mice. Three mice were used per genotype, two slices per mouse, all are displayed. Images for *Cox6c*, *Fam32*, *Gabra5*, *Oxr1*, *Nav1*, *Pla2g7*, *Pou6f1*, *PolB*, *Sgk1*, *Fosb*, *Nr4a3*, and *Xpb1* are shown. Due to space constraints all genes could not be shown.

Supplemental Table Legends

Table S2. Selected genes described in the text for the hippocampus. See also Figure 4. UP means positive fold-change and DOWN means negative fold-change.

Table S3. Selected genes described in the text for the OFBs. See also Figure 5. UP means positive fold-change and DOWN means negative fold-change.

Table 2. Selected genes described in the text for the hippocampus. See also Figure 4. UP means positive fold-change and DOWN means negative fold-change.

Gene	Differential Expression	Spatial Pattern	Description
Ubc	3xPBvsWT, 3xADvsWT (DOWN)	Global	Ubiquitin C
Gm10073	3xPBvsWT, 3xADvsWT (DOWN)	Global	Ribosomal protein, large, P1 pseudogene
Glo1	3xPBvsWT, 3xADvsWT (UP)	Global	Glyoxalase 1
Pkm	3xPBvsWT, 3xADvsWT (DOWN)	Global	Pyruvate kinase, muscle
Cox6c	3xPBvsWT, 3xADvsWT (DOWN)	Global	Cytochrome c oxidase subunit 6C
Rps2	3xPBvsWT, 3xADvsWT (DOWN)	Global	Ribosomal protein S2
Tmem59l	3xPBvsWT, 3xADvsWT (DOWN)	Global	Transmembrane protein 59-like
Gabra2	3xPBvsWT, 3xADvsWT (UP)	Global	Gamma-aminobutyric acid (GABA) A receptor, subunit alpha 2
Lpl	3xPBvsWT, 3xADvsWT (UP)	CA1, CA2-3	Lipoprotein lipase
Wbp11	3xPBvsWT, 3xADvsWT (UP)	Hippocampus	WW domain binding protein 11
Thy1	3xPBvsWT, 3xADvsWT (UP)	Global-CA3	Thymus cell antigen 1, theta
Bok	3xPBvsWT (DOWN)	CA2-3	BCL2-related ovarian killer
Rasl11a	3xADvsWT (DOWN)	CA2-3	RAS-like, family 11, member A
Paip1	3xPBvsWT (DOWN)	Global	Polyadenylate binding protein-interacting protein 1
Eif3f	3xPBvs3xAD (DOWN)	Global	Eukaryotic translation initiation factor 3, subunit F
Sgk1	3xPBvsWT, 3xPBvs3xAD (UP)	Global-hippocampus MCL/GCL - OB	Serum/glucocorticoid regulated kinase 1
Rpa2	3xPBvs3xAD (DOWN)	Global	Replication protein A2
Gadd45a	3xPBvs3xAD (UP)	Global	Growth arrest and DNA-damage-inducible 45 alpha
Cdkn1a	3xPBvs3xAD (UP)	Global-in 1 out of 3 mice	Cyclin-dependent kinase inhibitor 1A
Jun	PBvsWT-CA1 (DOWN), 3xPBvsWT-CA1 (UP)	DG	Jun D proto-oncogene

Table S3. Selected genes described in the text for the OFBs. See also Figure 5. UP means positive fold-change and DOWN means negative fold-change.

Gene	Differential Expression	Spatial Pattern	Description
Ubc	3xPBvsWT, 3xADvsWT (DOWN)	Global	Ubiquitin C
Gm10073	3xPBvsWT, 3xADvsWT (DOWN)	Global	Ribosomal protein, large, P1 pseudogene
Glo1	3xPBvsWT, 3xADvsWT (UP)	Global	Glyoxalase 1
Pla2g7	3xPBvsWT, 3xADvsWT (DOWN)	MCL	Phospholipase A2, group VII (platelet-activating factor acetylhydrolase, plasma)
Stk25	3xPBvsWT, 3xADvsWT (UP)	Global	Serine/threonine kinase 25 (yeast)
Ctss	3xPBvsWT, 3xADvsWT (UP)	Global	Cathepsin S
Fam32	3xPBvsWT, 3xADvsWT (UP)	Global	Family with sequence similarity 32, member A
Srp54b	3xPBvsWT, 3xADvsWT (UP)	Global	Signal recognition particle 54B
Gabra5	3xPBvsWT, 3xADvsWT (UP)	GCL	Gamma-aminobutyric acid (GABA) A receptor, subunit alpha 5
Oxr1	3xPBvsWT, 3xADvsWT (UP)	EPL,MCL	Oxidation resistance 1
Npr1	3xPBvsWT (UP)	MCL	Natriuretic peptide receptor 1
Nav1	3xPBvsWT, 3xADvsWT (UP)	EPL	Neuron navigator 1
Apold1	3xADvsWT (DOWN)	GL	Apolipoprotein L domain containing 1
Fosb	3xPBvsWT, 3xADvsWT (DOWN)	MCL, GCL	FBJ osteosarcoma oncogene B
Fos	3xPBvsWT, 3xADvsWT, PBvsWT (DOWN)	MCL,GCL	FBJ osteosarcoma oncogene
Junb	3xPBvsWT, 3xADvsWT (DOWN)	MCL,GCL	Jun B proto-oncogene
Egr4	3xPBvsWT, 3xADvsWT (DOWN)	MCL,GCL	Early growth response 4
Nr4a1	3xPBvsWT, 3xADvsWT (DOWN)	MCL,GCL	Nuclear receptor subfamily 4, group A, member 1
Nr4a3	3xPBvsWT, 3xADvsWT (DOWN)	MCL, GCL	Nuclear receptor subfamily 4, group A, member 3
Pou6f1	3xPBvsWT, 3xADvsWT (DOWN)	Global	POU domain, class 6, transcription factor 1
Homer1	3xPBvsWT, PBvsWT (UP)	MCL,GCL	Homer scaffolding protein 1
Sgk1	3xPBvsWT, 3xPBvs3xAD (UP)	Global, GCL	Serum/glucocorticoid regulated kinase 1
Xbp1	3xPBvsWT, 3xPBvs3xAD (UP)	Global	X-box binding protein 1

Transparent Methods

LEAD CONTACT AND MATERIALS AVAILABILITY

Further information and requests should be directed to and will be fulfilled by the Lead Contact, Vilhelm A. Bohr (vbohr@nih.gov). This study did not generate new unique reagents.

Mice

Mice, middle aged see below, were generated and maintained at the National Institute on Aging Intramural Research facility in Baltimore, MD. Generation of the 3xPB strain has been described previously (Sykora et al., 2015). All mice are on a C57BL/6J background. Mice were maintained on a standard NIH diet and a 12-h light/dark cycle. Mice were group housed and had ad libitum access to food and water. Littermates were always used as controls whenever possible. The LTP and brain hemispheres were from 12-16m male mice. Olfactory behavioral tests and the bulbs for ST were derived from 11-13m old male mice. For ST, three mice per genotype and two sections per mouse were included for analysis. All animal procedures were approved by the National Institute on Aging Animal Care and Use Committee and complied with NIH guidelines.

Immunohistochemistry for GFAP, IBA1 and Ab

Briefly, anesthetized mice were perfused with 1x PBS and then with freshly prepared 4% paraformaldehyde (PFA) in PBS. Two brains per genotype were used. Brains were placed in 4% PFA for 24 h and then equilibrated in 30% then 15% sucrose, sequentially overnight. Sixteen-micron thick brain sagittal sections were prepared via cryosectioning. The sagittal sections from each mouse were incubated with 1% hydrogen peroxide in PBS to block endogenous peroxidases then rinsed in PBS. The sections were washed and blocked using 5% normal goat serum (NGS: Jackson Immuno Research) in PBS+ (PBS plus 0.3% Triton X-100) for 30 min at room temperature. Thereafter, samples were incubated overnight with the primary antibody with 1% normal goat serum in PBS+ at 4°C. The primary antibodies and dilutions were GFAP (Z0334, DAKO, dilution 1:1000), IBA-1 (019-19741, Wako, dilution 1:1000); β -amyloid (2454S, Cell signaling, dilution 1:200). The slides were rinsed with PBS and incubated with biotinylated secondary donkey anti-rabbit secondary antibody in PBS donkey- α -rabbit IgG antibody (1:400; Jackson Immuno Research) for one hour. Slides were rinsed then incubated with ABC solution (Vectastain ABC kit, Vector) for 30 minutes. The sections were washed, stained using 0.04% 3,3'-Diaminobenzidine (DAB) and 0.01% H₂O₂ for 8 minutes and subsequently dehydrated using a sequence of different ethanol concentrations. The slides were kept in the dark and left to air dry for 30 minutes, mounted with coverslips using DePex (Serva) and stored at RT. Slides were scanned with NanoZoomer Digital Pathology system (Hamamatsu Photonics, K.K., Japan) with 40X objective.

ST tissue collection and processing

Adult mice were sacrificed and the brains were removed from the cranial cavity, embedded in OCT and snap-frozen in isopentane pre-cooled with dry ice and liquid nitrogen. Olfactory bulbs and the left hemispheres were not from the same mice. Brains were sectioned on the cryostat at 10 μ m thickness. Sections were placed on the spatially barcoded arrays with one section per well. Sections were fixed in 3.6-3.8% formaldehyde (Sigma) in PBS, washed in PBS, then treated for 1 min with isopropanol and air-dried. To stain the tissue, sections were incubated in Mayer's Hematoxylin (Dako) for 7 min, then Bluing buffer for 2 min and Eosin (Sigma) for 20 s. After drying, the slides were mounted with 85% glycerol and images of sections were taken using Metafer Slide Scanning Platform (Metasystems). Raw images were stitched together using VSlide software (Metasystems). To pre-permeabilize the tissue, sections were incubated for 30 min at 37°C with Exonuclease I Reaction Buffer (NEB) mixed with 0.2 μ g/ μ l BSA (NEB). Sections were incubated for 20 min at 37°C with 0.5 U/ μ l collagenase (ThermoFisher) in HBSS buffer mixed with 0.2 μ g/ μ l BSA (NEB). Following washing in 0.1x SSC buffer (Sigma). Sections were permeabilized with 0.1% pepsin/HCl (Sigma) at 37°C 10 and 6 min, respectively. Then, the sections were washed with 0.1x SSC buffer.

After permeabilization, a reverse transcription mix containing Superscript III reverse transcriptase (ThermoFisher) was added to each section and incubated overnight at 42°C as described previously (Stahl et al., 2016). Next, to remove tissue from the slide, sections were incubated for 1 h at 56°C with Proteinase K in PKD buffer (both from Qiagen). Surface probes with bound mRNA/cDNA were then cleaved from the slide by USER enzyme (NEB) (Stahl et al., 2016). Released probes were collected from each well and transferred to separate tubes. Next, 2nd strand synthesis, cDNA purification, in vitro

transcription, aRNA purification, adapter ligation, post-ligation purification, a second 2nd strand synthesis and purifications were carried out using an automated MBS 8000 system as described previously (Jemt et al., 2016). cDNA was amplified by PCR using Illumina Indexing primers (Stahl et al., 2016) and purified using carboxylic acid beads on an automated MBS robot system (Lundin et al., 2010). An Agilent Bioanalyzer High Sensitivity DNA Kit (Agilent) was used to analyze the size distribution of the final libraries. The concentration of the libraries was measured with Qubit dsDNA HS (ThermoFisher). Probes were collected from each well and transferred to separate tubes. Next, second strand synthesis, cDNA purification, in vitro transcription, aRNA purification, adapter ligation, post-ligation purification. The second strand synthesis and purification were carried out using an automated MBS 8000 system as described previously (Jemt et al., 2016). cDNA was amplified by PCR using Illumina Indexing primers (Stahl et al., 2016) and purified using carboxylic acid beads on an automated MBS robot system (Lundin et al., 2010). An Agilent Bioanalyzer High Sensitivity DNA Kit (Agilent) was used to analyze the size distribution of the final libraries. The concentration of the libraries was measured with Qubit dsDNA HS (ThermoFisher). After the probes were released from the slide surface, the features with remaining non-cleaved DNA probes were detected by incubation with hybridization mixture containing Cyanine-3 labelled oligonucleotides, as described previously (Stahl et al., 2016). Fluorescent images were acquired using the same microscope as for the bright field images.

Sequencing

The libraries were sequenced on the Illumina Nextseq platform using paired-end sequencing. Thirty bases were sequenced on read one to determine the spatial barcode and UMI, and 55 bases were sequenced on read two to cover the genetic region.

Image alignment and spot detection

Image alignment

Bright field stained images (HE) and fluorescent images (Cy3) were aligned using Adobe Photoshop CS6 by first down-sampling them by 40% and then overlaying both images using the transparency channels. The alignment was performed using common tissue features visible in both images when applying brightness and contrast filters. Aligned images were cropped to the borders of the array and a mask was created around the Cy3 image outside the tissue area, the images were then saved for the spot detection. The spot detection was performed with ImageJ where the spot centroids were detected using the analyze particles feature. Detected spot centroids (inside tissue) pixel coordinates were exported to a file. An R script was then used to convert the pixel coordinates to array coordinates and to assign these to an array position by rounding methods.

Data processing

Sequenced raw data was processed using the open source ST Pipeline v1.45 (Navarro et al., 2017) with the genome reference Ensembl GRCm38 v86 and reference Mouse GenCode vM11 (Comprehensive gene annotation). The ST Pipeline was executed with the following settings: enabled homopolymers filter (A,G,T,C,N) with a length of 10; enabled two-pass mode for the alignment step; removed non-coding RNA (using the latest (v86) non-coding RNA database from Ensembl); discarded reads whose UMI has more than 6 low quality bases; discarded trimmed reads shorter than 20. The matrices of counts (spots by genes) generated by the ST Pipeline were filtered to replace Ensembl IDs by gene names and to keep only protein-coding, long-non-coding-intergenic and antisense genes. The matrices of counts underwent another filtering step where only spots inside the tissue were kept using the file generated in the previous step (image alignment).

Sections alignment

Sections of each dataset (hippocampus and OFB) were aligned against each other using the ST Analysis package (https://github.com/jfnavarro/st_analysis).

Datasets

We created a total of 48 sections, 12 from the OFB and 12 the from hippocampus with two consecutive sections per mouse (technical replicates).

Factor Analysis

A joint factor analysis (Maaskola et al., 2018) was performed separately for the OFB and hippocampus datasets. The genotype and section number were used as covariates to adjust for batch effects. We used version 0.4 of the software with the following parameters: adjdepth, stage 50, minread_spot 10, dropout 0.2, optimization adam_nesterov. The factor analysis generates factors activities for each spot. Factors usually correspond to different regions in a uniform and unbiased way. The OFB dataset was processed to compute 10 factors, the hippocampus dataset was processed to compute 20 factors. We clustered hierarchically the factor activities of each dataset, this resulted in 14 clusters (hippocampus) and 5 clusters (OFB).

UMAP visualization

Factor activities were reduced to a 2D manifold using the ST Analysis package, the same package was used to colour the manifolds by cluster and other covariates (genotype, animal and chip).

Differential Expression Analysis

Two differential expression analyses were performed separately for each dataset (OFB and hippocampus). Spots whose total count was below 200 were discarded. Similarly, genes that were detected (count > 0) in less than 10% of the spots were also discarded. For the OFB dataset spots for each cluster were sub-sampled in order to have a maximum of 20 spots per cluster (region) and genotype, this was repeated 12 times and only the genes that were detected 6 out of 12 times were kept. The R package DESeq2 (Love et al., 2014) was the tool used to perform the differential expression analysis with the following settings: useT=TRUE, minmu=1e-6, sfType="poscounts", minReplicates ForReplace=Inf, test="Wald".

Adjusted p-values and log₂-fold-changes were computed in two different ways. A genotype-based analysis for each cluster (PB vs WT, 3xPB vs WT, 3xAD vs WT, and 3xPB vs 3xAD) and a cluster-based analysis for each genotype (one vs rest). An adjusted p-value of 0.1 and an absolute log₂-fold-change of 0.5 were used as confidence thresholds.

Enrichment Analysis

Enrichment analysis was performed using Enrichr (Kuleshov et al., 2016) for gene sets and FGSEA (Korotkevich et al., 2016) for spots, both using default settings.

Long-term Potentiation Analysis (LTP)

Hippocampal slices were prepared as described previously (Zhang et al., 2011). Briefly, the mice were euthanized with isoflurane and brains were rapidly removed. Transverse slices were cut at a thickness of 350 µm. Prior to initiating recordings, the slices were allowed to recover for at least 1h in artificial cerebrospinal fluid (ACSF) at room temperature. ACSF (120 mM NaCl, 2.5 mM KCl, 1.25 mM NaH₂PO₄, 26 mM NaHCO₃, 1.3 mM MgSO₄, 2.5 mM CaCl₂, and 10 mM glucose (pH 7.4)) had 95/5% O₂/CO₂ bubbled through it prior to and during recovery. The osmolarity of the ACSF was adjusted to 290 milliosmoles using a 5600 Vapor Pressure Osmometer (Wescor, Inc). For recordings, stimuli (30 ms, every 20 s) were delivered by a fine bipolar tungsten electrode to activate Schaffer collateral/commissural afferents. LTP was induced with a burst of titanic stimulation (100 Hz for 1 s). All recordings were performed at 30-32 °C. Data was collected using a MultiClamp 700B amplifier (Molecular Devices). Signals were filtered at 2kHz and digitized at 10kHz with a Digidata 1440A Data Acquisition System and analyzed using (pCLAMP 10)/Clampfit 10 software (Molecular Devices). Graphic and statistics were prepared using SigmaPlotv14.

Buried Cookie Olfactory Test

This test was designed to study the ability of mice to find buried food after 16 hours of starvation and is dependent on their ability to smell the buried food pellet, and similar to what we did previously with slight modifications (Misiak et al., 2017). Each animal was tested in an individual cage with clean 2-inch-high bedding and a fixed amount of food pellet at the bottom of the bedding. Before the experiment, a food pellet used in this test was given to the animals as food to study the consumption relative to their regular diet pellet as well as to familiarize the mice with the smell of the food. During the test, each mouse was

given a 5 min period (600 sec) to find the buried food pellet. All tests were recorded, and we calculated the the latency of extracting the buried food under the bedding. After the olfactory tests, mice were processed for LTP. Graphic was prepared using GraphPad Prism v7.04, and statistics were derived from a one-way ANOVA.

Western Blotting

Brains were removed, dissected and immediately snap-frozen in liquid nitrogen. Protein extracts were prepared from the mouse cortex. Samples were lysed in RIPA buffer (Sigma) with protease inhibitor cocktail (Roche). Protein concentrations were measured by BCA assay (Thermo) and lysates were separated on 4-15% SDS PAGE and transferred to PVDF membrane. The membrane was incubated with blocking solution (5% non-fat dry milk in TBST) for 1 hr at room temperature, then with primary antibodies (Glo1 (1:1000 ABclonal A1932) or GloII (1:1000 Santa Cruz sc-166781) overnight at 4 °C. The membranes were incubated with HRP-conjugated secondary antibody (1:10,000) for 1h at room temperature and immunoreactivity was detected with an ECL kit (Thermo). Optical densities of the gels were quantified using BioRad's Image Lab software. Statistic calculations were done using GraphPad Prism v7.04 using a one-way ANOVA with Dunnett's post hoc test for multiple comparisons.

Proteomics analyses by high-end mass spectrometry

Mouse brain tissue samples from OFB of middle-aged female mice (8-12m) were analyzed by electrospray-based high-resolution mass spectrometry (MS) (Q-Exactive, Thermo Scientific, Germany) coupled directly to a nano liquid-chromatography (nLC) (EASY 1000, Thermo Scientific, Germany) for protein identification and quantification. Four biological replicates were used for each mice genotype, in total 16 mice brain tissue samples were analyzed by mass spectrometry. The tissue samples were lysed as previously described in (Lillenes et al., 2016). Protein lysates (50 ug) were further used for protein digestion with the filter-aided-sample-preparation (FASP). The protein samples were reduced in 1 mM dithiothreitol followed by rinsing on the filter with 8M urea. Next, the samples were alkylated with 50 mM iodoacetamide, with subsequent wash with 8 M urea and then with 50 mM Tris-HCl pH8.5. The proteins were digested on the filter with 1:50 of trypsin (Porcine origin sequencing grade modified, Promega) overnight in a wet chamber with gentle shaking. The peptides were collected by wash with 50 mM Tris-HCl pH8.5. The collected peptides were acidified to 0.1% trifluoroacetic acid and purified on C₁₈ material by use of StageTip columns. The purified peptides were resuspended in 0.1% formic acid. Each peptide sample was injected in duplicates of 650 ng to the nLC-MS/MS. A 330-minute gradient was used for peptide separation on the nLC and a data-dependent Top10 method for the MS/MS analysis. nLC-MS/MS results were searched using MaxQuant (version 1.6.0.16) against the mus musculus proteome (uniprot ID: UP000000589). Further processing of the identified and quantified values was performed in Perseus (version 1.6.1.3). For t-test calculations a threshold of 0.01 of permutation based false discovery rate (FDR) and minimum 3 valid values in at least one group was applied in Perseus. The mass spectrometry proteomics data are available via ProteomeXchange (Vizcaino et al., 2016) with identifier PXD017766.

Human Brains

Human brain samples were obtained from the Lille Neurobank, which was given to the French Research Ministry by the Lille Regional Hospital (CHRU-Lille) on August 14, 2008 under the reference DC- 2000-642. The Lille Neurobank fulfills criteria from the French Law on biological resources, including informed consent, ethics review committee, and data protection (article L1243- 4 du Code de la Santé publique, August 2007).

BOK analysis in human AD brains

Immunofluorescence was performed as described previously (Violet et al., 2015) using the following antibodies: AT8 (Thermo Scientific) is a phospho-dependent antibody which recognizes the phosphorylated Ser202/pThr205 epitope of Tau, and the anti-Bok (LSBio) were used. DAPI was used as a chromatin counterstain. Sagittal brain slices (5 µM) were deparaffinized and unmasked using citrate buffer (3.75 mM acid citrate, 2.5 mM disodium phosphate, pH 6) for 8 min in a pressure cooker. The slices were submerged for 1 h in 1% horse serum (Vector Laboratories), and the primary antibodies were incubated overnight at 4°C in the presence of PBS-0.2% Triton. The following primary antibodies were used: AT8, a phospho-dependent antibody which recognizes the phosphorylated Ser202/pThr205 epitope

of Tau (ThermoFisher Scientific)(1/400), and the anti-Bok (LSBio)(1/100). These antibodies were revealed via secondary antibodies coupled to Alexa 488 or 568 (Life Technologies) 1/1000 overnight. The sections were counterstained and mounted with Vectashield/DAPI (Vector Laboratories). DAPI was used as a chromatin counterstain.

Hippocampal and thalamic sections from control and AD brains (n = 3 per category) were acquired using an LSM 710 confocal laser-scanning microscope (Carl Zeiss). The confocal microscope was equipped with a 488-nm Argon laser, 561-nm diode-pumped solid-state laser, and a 405-nm ultraviolet laser. The images were acquired using an oil 63X Plan-APOCHROMAT objective (1.4 NA). All recordings were performed using the appropriate sampling frequency (16 bits, 1024–1024 images, and a line average of 4). Serial sections from the three-dimensional reconstruction were acquired using Z-steps of 0.2 μ m. For each section, cellular and nuclear (based on DAPI detection) fluorescence of CA cells were quantified using the FIDJI macro application of ImageJ (confocal microscopy platform, IMPRT, Institut de Médecine Prédictive et de Recherche Thérapeutique, Lille, France). Fluorescence intensity per cell is reported. Quantification corresponds to the z stack of serial confocal sections covering the entire thickness (5 μ m) of the brain section. Cellular or nuclear fluorescence was quantified in CA3 sections from three different control and AD brains. Control brains were set to 100%. Two-tailed, unpaired *t*-test was used for statistical analysis of immunofluorescence labeling. Data presented on a per cell basis as mean \pm SEM. The statistical significance calculation was derived from the mean value of each control and AD brain (n=3 per category).

Human validation datasets

The single-nuclei RNA-seq human dataset (AD) t-SNE plots of the parietal lobe were obtained using the ST analysis package with the data and annotations provided by Del-Aguila et al. (Del-Aguila et al., 2019). The single nuclei RNA-seq human dataset (AD and control) UMAP plots of the entorhinal cortex were obtained from the public web service (<http://adsn.ddnetbio.com/>) provided by Grubman et al. (Grubman et al., 2019).

Single-molecule RNA in situ hybridization

RNA in situ hybridization experiments were performed using the RNAscope® technology, which has been previously described (Wang et al., 2012). Paired double-Z oligonucleotide probes were designed against target RNA using custom software. The following probes were used: Mm-Gabra2, cat no. 435018, NM_008066.3, 20 pairs, nt 189-1171; Mm-Bok-C2, cat no. 801868-C2 NM_016778.3, 20 pairs, nt 486-1443; Mm-Lpl-C3, cat no. 402798-C3, NM_008509.2, 20 pairs, nt 448-1408. The RNAscope LS Multiplex Fluorescent Reagent Kit (cat. no. 322800) (Advanced Cell Diagnostics, Newark, CA) were used according to the manufacturer's instructions. Fresh frozen tissue sections were prepared according to the manufacturer's recommendations. Samples were post-fixed for 90 minutes using 10% neutral buffer formalin at RT prior to RNAscope. The pretreatment conditions for RNAscope LS are as follows: 30 minutes of protease IV at room temperature. Opal 520 (cat. no. FP1487001KT), Opal 570 (cat. no. FP1488001KT) and Opal 690 (cat. no. FP1497001KT) (Akoya Biosciences, Menlo Park, CA) were used at concentrations of 1:500, 1:1500, and 1:1500, respectively. Each sample was quality controlled for RNA integrity with a 3-plex mouse positive control probe (cat no. 320888). Negative control background staining was evaluated using a probe specific to the bacterial *dapB* gene. Fluorescent images were acquired using a 3D Histech Scanner. Three mice per genotype were submitted, but for technical reasons beyond our control, we were unable to obtain complete hippocampal images for 3xPB mice. Images were acquired from the same slide under identical conditions.

Data availability

Processed and analyzed data and analysis scripts generated during this study are available at Mendeley <https://doi:10.17632/6s959w2zyr.1> and GitHub https://github.com/jfnavarro/AD_POLB_ST. The mass spectrometry proteomics data have been deposited to the ProteomeXchange Consortium via the PRIDE (PubMed ID: 30395289) partner repositories with the dataset identifier PXD017766.

Supplemental References

- Del-Aguila, J.L., Li, Z., Dube, U., Mihindikulasuriya, K.A., Budde, J.P., Fernandez, M.V., Ibanez, L., Bradley, J., Wang, F., Bergmann, K., et al. (2019). A single-nuclei RNA sequencing study of Mendelian and sporadic AD in the human brain. *Alzheimers Res Ther* 11, 71.
- Grubman, A., Chew, G., Ouyang, J.F., Sun, G., Choo, X.Y., McLean, C., Simmons, R.K., Buckberry, S., Vargas-Landin, D.B., Poppe, D., et al. (2019). A single-cell atlas of entorhinal cortex from individuals with Alzheimer's disease reveals cell-type-specific gene expression regulation. *Nat Neurosci* 22, 2087-2097.
- Jemt, A., Salmén, F., Lundmark, A., Mollbrink, A., Fernández Navarro, J., Ståhl, P.L., Yucel-Lindberg, T., and Lundeberg, J. (2016). An automated approach to prepare tissue-derived spatially barcoded RNA-sequencing libraries. *Scientific Reports* 6, 37137.
- Korotkevich, G., Sukhov, V., and Sergushichev, A. (2016). Fast gene set enrichment analysis. *bioRxiv* 19 Jun 2016.
- Kuleshov, M.V., Jones, M.R., Rouillard, A.D., Fernandez, N.F., Duan, Q.N., Wang, Z.C., Koplev, S., Jenkins, S.L., Jagodnik, K.M., Lachmann, A., et al. (2016). Enrichr: a comprehensive gene set enrichment analysis web server 2016 update. *Nucleic Acids Research* 44, W90-W97.
- Lillenes, M.S., Rabano, A., Stoen, M., Riaz, T., Misaghian, D., Mollersen, L., Esbensen, Y., Gunther, C.C., Selnes, P., Stenset, V.T., et al. (2016). Altered DNA base excision repair profile in brain tissue and blood in Alzheimer's disease. *Mol Brain* 9, 61.
- Love, M.I., Huber, W., and Anders, S. (2014). Moderated estimation of fold change and dispersion for RNA-seq data with DESeq2. *Genome Biol* 15, 550.
- Lundin, S., Stranneheim, H., Pettersson, E., Klevebring, D., and Lundeberg, J. (2010). Increased throughput by parallelization of library preparation for massive sequencing. *Plos One* 5, e10029.
- Maaskola, J., Bergenstrahle, L., Jurek, A., Navarro, J.F., Lagergren, J., and Lundeberg, J. (2018). Charting Tissue Expression Anatomy by Spatial Transcriptome Decomposition. *bioRxiv* doi: <https://doi.org/10.1101/362624>.
- Misiak, M., Vergara Greeno, R., Baptiste, B.A., Sykora, P., Liu, D., Cordonnier, S., Fang, E.F., Croteau, D.L., Mattson, M.P., and Bohr, V.A. (2017). DNA polymerase beta decrement triggers death of olfactory bulb cells and impairs olfaction in a mouse model of Alzheimer's disease. *Aging Cell* 16, 162-172.
- Navarro, J.F., Sjostrand, J., Salmen, F., Lundeberg, J., and Stahl, P.L. (2017). ST Pipeline: an automated pipeline for spatial mapping of unique transcripts. *Bioinformatics* 33, 2591-2593.
- Stahl, P.L., Salmen, F., Vickovic, S., Lundmark, A., Navarro, J.F., Magnusson, J., Giacomello, S., Asp, M., Westholm, J.O., Huss, M., et al. (2016). Visualization and analysis of gene expression in tissue sections by spatial transcriptomics. *Science* 353, 78-82.
- Sykora, P., Misiak, M., Wang, Y., Ghosh, S., Leandro, G.S., Liu, D., Tian, J., Baptiste, B.A., Cong, W.N., Brennerman, B.M., et al. (2015). DNA polymerase beta deficiency leads to neurodegeneration and exacerbates Alzheimer disease phenotypes. *Nucleic Acids Res* 43, 943-959.
- Violet, M., Chauderlier, A., Delattre, L., Tardivel, M., Chouala, M.S., Sultan, A., Marciniak, E., Humez, S., Binder, L., Kaye, R., et al. (2015). Prefibrillar Tau oligomers alter the nucleic acid protective function of Tau in hippocampal neurons in vivo. *Neurobiol Dis* 82, 540-551.
- Vizcaino, J.A., Csordas, A., del-Toro, N., Dianas, J.A., Griss, J., Lavidas, I., Mayer, G., Perez-Riverol, Y., Reisinger, F., Ternent, T., et al. (2016). 2016 update of the PRIDE database and its related tools. *Nucleic Acids Res* 44, D447-456.
- Wang, F., Flanagan, J., Su, N., Wang, L.C., Bui, S., Nielson, A., Wu, X., Vo, H.T., Ma, X.J., and Luo, Y. (2012). RNAscope: a novel in situ RNA analysis platform for formalin-fixed, paraffin-embedded tissues. *J Mol Diagn* 14, 22-29.
- Zhang, J., Wang, Y., Chi, Z., Keuss, M.J., Pai, Y.M., Kang, H.C., Shin, J.H., Bugayenko, A., Wang, H., Xiong, Y., et al. (2011). The AAA+ ATPase Thorase regulates AMPA receptor-dependent synaptic plasticity and behavior. *Cell* 145, 284-299.